On radar imaging of current features: 1. Model and comparison with observations

V. Kudryavtsev,[1,2] D. Akimov,[3] J. Johannessen,[4,5] and B. Chapron[6]

[1] A new radar imaging model of ocean current features is proposed. The simulated normalized radar cross section (NRCS) takes into account scattering from ''regular'' surfaces (by means of resonant Bragg scattering and specular reflections) and scattering from breaking waves. The description of background wind waves and their transformation in nonuniform medium is based on solution of the wave action conservation equation. Wave breaking plays a key role in the radar imaging model. Breaking waves scatter radio waves (thus directly contributing to the NRCS), provide energy dissipation in wind waves (thus defining the wave spectrum of intermediate scale waves), and generate short surface waves (thus affecting Bragg scattering). Surface current, surfactants accumulated in the convergence zone, and varying wind field are considered as the main sources for the NRCS manifestations of current features. The latter source can result from transformation of atmospheric boundary layer over the sea surface temperature front. It is shown that modulation of wave breaking significantly influences both radar returns and short wind waves. In the range of short gravity waves related to Ku- X-, and C-bands, the modulation of Bragg waves through wave breaking is the governing mechanism. The model is tested against well-controlled experiments including JOWIP, SARSEX, and CoastWatch-95. A reasonably good agreement between model and observations is obtained.

Citation: Kudryavtsev, V., D. Akimov, J. Johannessen, and B. Chapron (2005), On radar imaging of current features: 1. Model and comparison with observations, *J. Geophys. Res.*, *110*, C07016, doi:10.1029/2004JC002505.

1. Introduction

[2] Manifestation of ocean surface features such as meandering fronts with convergence and divergence zones, eddies, and internal waves have been regularly observed and documented in SAR images since the SEASAT L-band SAR in 1978 [*Beal et al.*, 1981]. Wave-current interactions, suppression of short wind wave by surfactants (accumulated in the current convergence), and varying wind field resulting from the transformation of the atmospheric boundary layer across sea surface temperature front are commonly accepted as mechanisms responsible for the manifestation of such ocean features [e.g., *Marmorino et al.*, 1994; *Johannessen et al.*, 1996; *Espedal et al.*, 1998; *Beal et al.*, 1997; *Chubb et al.*, 1999; *Cooper et al.*, 1994; *Vogelzang et al.*, 1991; *Hughes and Dawson*, 1988; *Gasparovich et al.*, 1988].

[3] Radar imaging models combine microwave scattering with the wave action (energy) conservation equation written in relaxation approximation [e.g., *Hughes*, 1978; *Thompson et al.*, 1988; *Lyzenga and Bennett*, 1988]. The main difference between the models relates to the description of radar scattering and the parameterization of the relaxation rate. One of the first imaging models proposed by *Alpers and Hennings* [1984] was based on the Bragg scattering theory, and they revealed that such models dramatically underestimate observed radar signatures at all radar frequencies above perhaps L-band. The reason for this is that the relaxation rate of shorter gravity waves, such as for C-band, is very fast and thus prohibited to be modulated by typical current gradients with a width of the order of 1 km.

[4] Building on the Bragg scattering theory, radar imaging models have gradually evolved and improved following the introduction of the integral equation method [*Holliday et al.*, 1986] and the composite scattering modeling [*Lyzenga and Bennett*, 1988; *Thompson*, 1988]. In short, these models indicated that intermediate scale waves carrying the shorter Bragg waves play a crucial role in the formation of radar signatures. Through changes in tilt modulation and specular reflection imposed by current gradients, the inclusion of these longer waves with weaker relaxation rate reduces the gap between simulated and observed radar cross-section anomalies. However, in spite of general improvement, discrepancies were still significant in several specific cases regarding imaging of internal waves and tidal currents on shallow water [see, e.g., *Romeiser and Alpers*, 1997; *Lyzenga and Bennett*, 1988; *Cooper et al.*, 1994].

[5] Several authors suggested that this discrepancy might be explained by the effect of wave breaking on microwave scattering. Using experimental findings by *Walker et al.*

---

[1]Marine Hydrophysical Institute, Sebastopol, Ukraine.
[2]Also at Nansen Environmental and Remote Sensing Center, Bergen, Norway.
[3]Nansen International Environmental and Remote Sensing Center, St. Petersburg, Russia.
[4]Nansen Environmental and Remote Sensing Center, Bergen, Norway.
[5]Also at Geophysical Institute, University of Bergen, Bergen, Norway.
[6]Institute Francais de Recherche pour l'Exploitation de la Mer, Plouzane, France.

[1996] for stationary wave breakers, *Lyzenga* [1996] related the generation of short surface waves to energy dissipation due to breaking of longer waves. Assuming that wave breaking imposes a hard upper limit to wave spectrum, he found that energy input from the current gradient causes additional energy dissipation which in turn results in enhancement of shorter gravity waves, in particular Bragg waves. His estimates qualitatively showed that this effect might have an important contribution to radar signatures of current gradients.

[6] Moreover, in studies by *Chubb et al.* [1999] and *Jansen et al.* [1998] effect of wave breaking was accounted for through their direct contribution to radar scattering. They incorporated microwave scattering from individual breakers at grazing angles proposed by *Wetzel* [1986], and statistics of wave breaking based on the threshold level approach developed by *Snyder and Kennedy* [1983]. After a tuning of the model parameters, they reached an agreement between model prediction and radar signatures of the Gulf Stream current convergence fronts. However, the model possesses some internal inconsistencies. First, expression for the individual breaker radar cross section obtained by *Wetzel* [1986] for grazing angles is extrapolated and used in the radar imaging model at arbitrary incidence angles. Second, the energy dissipation due to wave breaking is proportional to the spectrum square without any justification. Finally, the wave breaking process is described by a very different manner in the electromagnetic and the wave action conservation components of the radar imaging model.

[7] In the present study we propose a radar imaging model of current features based on the normalized radar cross section (NRCS) model by *Kudryavtsev et al.* [2003a]. Statistical properties of the sea surface results from solution of the energy balance equation where wind forcing, viscous and wave breaking dissipation, wave-wave interactions, and generation of short waves by breaking waves of longer scales are taken into account. The latter mechanism is described by *Kudryavtsev and Johannessen* [2004], and though it does not significantly alter the background wave spectrum, it plays a crucial role in the context of wave modulations by a surface current. In this paper the same energy balance equation is used for description of both the background surface and its disturbances caused by surface current features. Unlike previous studies, the same wave breaking statistics (length of the wave breaking crest) proposed by *Phillips* [1985] is adopted in the wave energy balance equation and the radio wave scattering model. This ensures a consistent description of the radio wave scattering and hydrodynamic component of the radar imaging model in the context of energy dissipation and wave breaking.

[8] The background NRCS model has been extensively verified on available data obtained at different geometry. *Kudryavtsev et al.* [2003b] applied the background model for the radar modulation transfer function (MTF) studies. In the present study we make further improvement and extend the model to imaging of surface current features. The model with key new formulations is presented in sections 2, 3, and 4, followed by the model validation by existing airborne radar signatures of internal waves (JOWIP [*Hughes and Dawson*, 1988] and SARSEX [*Gasparovich et al.*, 1988]) and ERS-1/2 satellite SAR radar signatures of the Norwegian Coastal

Current (CoastWatch-95 experiment [*Johannessen et al.*, 1997]) in section 5. The conclusion is given in section 6. Note that in the present study we do not consider SAR imaging artifacts (such as velocity bunching). Thus the proposed model is de facto a real aperture radar imaging model.

2. Radar Scattering From the Sea Surface

[9] The primary challenge in radar image modeling is the need to ensure consistency between the parameterization of scattering mechanisms and the physical characterization of sources and sinks in the wave action conservation equation. This is respectively addressed in the sections 2.1 and 2.2, followed by a brief comparison with empirical results in section 2.3.

2.1. Governing Equations for Radar Scattering

[10] Following the background NRCS model by *Kudryavtsev et al.* [2003a], the sea surface is represented as a "regular" (nonbreaking) wavy surface combined with a number of breaking zones. It is well known that breaking waves provide a strong spike-like radar signal. Though the fraction of the sea surface covered by breaking waves is usually small, they may nevertheless significantly contribute to the NRCS. Radar scattering from the regular surface and from the wave breaking zones are statistically independent. Thus the NRCS of the sea surface can be presented as a sum,

$$\sigma_0^p = \sigma_{0R}^p(1-q) + \sigma_{0b}q, \tag{1}$$

where σ_{0R}^p and σ_{0b} are the NRCS of the regular surface and a wave breaking zone correspondingly, and q is fraction of the sea surface covered by breaking zones.

[11] Radar scattering from the regular surface is described within the frame of the composite model combining specular reflection and resonant (Bragg) scattering mechanisms. The composite model was first derived from physical arguments by *Valenzuela et al.* [1971], and derived rigorously by *Bahar* [1981], and later by *Thompson* [1988]. It reads

$$\sigma_{0R}^p(\theta) = \pi R^2 \sec^4\theta \cdot P(\eta_i, \eta_n)\Big|_{\substack{\eta_i = \tan\theta \\ \eta_n = 0}}$$
$$+ \int_\Gamma \sigma_{0br}^p(\theta - \eta_i)P(\eta_i)d\eta_i, \tag{2}$$

where θ is the incidence angle; R^2 is an effective Fresnel reflection coefficient; $P(\eta_i)$ and $P(\eta_i, \eta_n)$ are one- and two-dimensional probability density functions of the sea surface slope in the direction of the incidence plane (η_i) and in the orthogonal direction (η_n); σ_{0br}^p is the Bragg scattering NRCS expressed as

$$\sigma_{0br}^p(\theta') = 16\pi k_r^4|G_P(\theta')|^2 S_r(k_b, \varphi), \tag{3}$$

where k_r is the radio wave number; $\theta' = \theta - \arctan(\eta_i)$ is the local incidence angle (which can be approximated by $\theta' = \theta - \eta_i$ for small slopes); φ is the azimuth (radar look direction) relative to the wind direction; $|G_p|^2$ is the geometric scattering coefficients (their expressions are

given by, for example, *Plant* [1990]); $k_b = 2k_r \sin\theta'$ is the local wave number of the Bragg waves; and $S_r(k_b, \varphi)$ is the wave number (folded) spectrum of the surface elevations.

[12] In composite models the wave spectrum is divided in two intervals: small-scale waves $k > k_d$ (with elevation variance h_s^2) and large-scale waves $k < k_d$. The dividing wave number is $k_d = d \cdot k_r$, where d is a constant less than unit. In this study we choose $d = 1/4$ in close agreement with *Thompson* [1988]. Small-scale waves with $k > k_d$ provide resonant scattering, while large-scale waves affect the scattering via random changes in the local incidence angle and rotation of the incidence plane. Resonant scattering takes place on the surface patches where the local Bragg wave number exceeds k_d, i.e., where the condition

$$2k_r \sin|\theta - \arctan(\eta_i)| \geq k_d \qquad (4)$$

is fulfilled. This condition defines domain of integration over the surface slopes Γ in the second term of (2).

$$\Gamma = [\eta_i \leq \tan(\theta - d/2) \cup \eta_i \geq \tan(\theta + d/2)]. \qquad (5)$$

To obtain (5) we used the fact that quantity $d/2$ is small. The surface patches where condition (4) is not fulfilled (or $\eta_i \notin \Gamma$) do not contribute to the radar return by means of the Bragg scattering, but provide radar return due to the specular reflection (the first term in (2)). In this case, small-scale roughness reduces the nominal Fresnel reflection coefficient by factor: $\exp(-4k_r^2 h_s^2)$ [e.g., *Holliday et al.*, 1986; *Thompson*, 1988].

[13] Note the following. First, in Bragg scattering component we do not account for the effect of tilt across the incidence plane. As shown by *Plant* [1990], this effect is negligible for VV-polarization. In HH-polarization this effect slightly modifies the geometric coefficient $|G(\theta - \eta_i, \eta_n)|^2$. However, it does not contribute significantly to the NRCS at small and moderate incidence angles [see, e.g., *Kudryavtsev et al.*, 2003a, Figure 5]. Second, additional impact on resonant scattering may come from hydrodynamic modulations of Bragg waves by longer surface waves. Model calculations done by, for example, *Kudryavtsev et al.* [2003a] showed that this effect is not strong (it gives only some upwind/downwind difference) and can be omitted in the radar imaging problem. Third, at moderate incidence angle, the integral in (2) can be effectively evaluated due to expansion of the integrand into Taylor series up to the second order. This was done in the background NRCS model and in, for example, the model by *Romeiser and Alpers* [1997]. However, at $\theta < (20° - 25°)$ (that is, the case of SAR observations), this expansion very quickly loses its validity [see, e.g., *Kudryavtsev et al.*, 2003a, Figure 6].

[14] Regarding the specular reflection, it is usually accepted that the probability density function of the sea surface slope is near Gaussian. The two-dimensional probability density function for the surface slopes in the incidence plane and in the orthogonal direction reads

$$P(\eta_i, \eta_n) = \frac{1}{2\pi\sqrt{\Delta_2}} \exp\left(-\frac{\overline{\eta_n^2}\eta_i^2 - 2\overline{\eta_i\eta_n}\eta_i\eta_n + \overline{\eta_i^2}\eta_n^2}{2\Delta_2}\right), \quad (6)$$

where $\Delta_2 = \overline{\eta_n^2\eta_i^2} - (\overline{\eta_i\eta_n})^2$ is the determinant of the covariance matrix. Elements of this matrix are related to the upwind s_{up}^2 and cross-wind s_{cr}^2 mean square slopes as

$$\overline{\eta_i^2} = s_{up}^2 \cos^2\varphi + s_{cr}^2 \sin^2\varphi, \qquad (7)$$

$$\overline{\eta_n^2} = s_{cr}^2 \cos^2\varphi + s_{up}^2 \sin^2\varphi, \qquad (8)$$

$$\overline{\eta_i\eta_n} = \left(s_{up}^2 - s_{cr}^2\right)\cos\varphi\sin\varphi, \qquad (9)$$

where φ is the radar look direction in respect to the wind velocity vector. Using (7)–(9), it is easy to check that the covariance matrix is invariant in respect to the radar look direction φ and equal to $\Delta_2 = s_{up}^2 s_{cr}^2$. Then accounting for the conditions of specular reflection ($\eta_i = \tan\theta, \eta_n = 0$), the first term of (2) is reduced to

$$\pi R^2 \sec^4\theta P(\eta_i, \eta_n)\bigg|_{\substack{\eta_i = \tan\theta \\ \eta_n = 0}} = \frac{\pi R^2 \sec^4\theta}{s_{up}s_{cr}} \exp\left(-\frac{\tan^2\theta}{2s_{sp}^2}\right),$$

$$(10)$$

where $s_{sp}^2 = s_{up}^2 s_{cr}^2/(s_{up}^2 \sin^2\varphi + s_{cr}^2 \cos^2\varphi)$ is the mean square slope satisfying conditions of the specular reflections.

[15] The second term in (1) describes contribution of wave breaking to the sea surface NRCS. As suggested by *Kudryavtsev et al.* [2003a], the radar scattering from an individual breaking zone can be described as specular reflections from very rough wave breaking patterns, and only breaking of waves with wave numbers much less (in 10 and more times) than k_r can contribute to the radio wave scattering. The NRCS of an individual wave-breaking zone is

$$\sigma_{0b}(\theta, \varphi) = \sigma_{0wb}(\theta)\left(1 + M_{wb}\overline{\theta}_{wb}A_{wb}(\varphi)\right), \qquad (11)$$

where σ_{0wb} is similar to (10) and reads

$$\sigma_{0wb} \propto \left(\sec^4\theta/s_{wb}^2\right)\exp\left(-tg^2\theta/s_{wb}^2\right) + \varepsilon_{wb}/s_{wb}^2. \qquad (12)$$

Here s_{wb}^2 is the mean square slope of the breaking zone roughness (which is assumed isotropic); ε_{wb} is the ratio of vertical to horizontal scale of the breaking zone; $M_{wb} = (1/\sigma_{0wb})d\sigma_{0wb}/d\theta$ is a tilting transfer function; $\overline{\theta}_{wb}$ is mean tilt of wave breaking zones; and $A_{wb}(\varphi)$ is the angular distribution of scattering from breaking waves, providing, in particular, the NRCS upwind/downwind difference. The geometrical properties of breaking waves are self-similar [*Phillips*, 1985], therefore s_{wb}^2 and ε_{wb} universal constants are chosen so as to fit the measurements, i.e., $s_{wb}^2 = 0.19$, $\varepsilon_{wb} = 5 \cdot 10^{-3}$.

[16] To calculate the NRCS in (1) with (11) and (12), one needs to know the spectrum of Bragg waves, the mean square slope, and fraction of the sea surface covered by breaking areas. At a given spectrum the up- and cross-wind components of the mean square slope are

$$s_{up}^2 = \int_{k<k_d} k_1^2 k^{-4} B(\mathbf{k}) d\mathbf{k}$$

$$s_{cr}^2 = \int_{k<k_d} k_2^2 k^{-4} B(\mathbf{k}) d\mathbf{k}$$

$$(13)$$

where $B(\mathbf{k})$ is the saturation spectrum. As shown below, the fraction of the sea surface q covered with breaking waves is also related to this saturation spectrum. To complete the model, we need to quantify the wave spectrum, and its transformation in the presence of a changing current, varying wind field and surfactants that result in the manifestation of surface current features in radar images.

2.2. Model of the Wind Wave Spectrum

2.2.1. Governing Equations

[17] The description of the wave spectrum is based on the energy balance equation which is more convenient to use in terms of the wave action spectrum $N(\mathbf{k})$ [e.g., *Phillips*, 1977],

$$\frac{\partial N(\mathbf{k})}{\partial t} + \left(c_{gi} + u_i\right)\frac{\partial N(\mathbf{k})}{\partial x_i} - k_j\frac{\partial u_j}{\partial x_i}\frac{\partial N(\mathbf{k})}{\partial k_i} = Q(\mathbf{k})/\omega, \quad (14)$$

where c_{gi} and u_i are components of the wave group velocity and the surface current (i and j = 1, 2), ω and $\mathbf{k}$ are the intrinsic frequency and wave number vector related by the dispersion relation

$$\omega^2 = gk + \gamma k^3, \quad (15)$$

$k = |\mathbf{k}|$, g is the gravity acceleration, γ is the surface tension, and $Q(\mathbf{k})$ is the source of wave energy. The wave height spectrum $F(\mathbf{k})$, energy spectrum $E(\mathbf{k})$, and wave action spectrum $N(\mathbf{k})$ are related via $E(\mathbf{k}) = (\omega^2/k)F(\mathbf{k})$, and $N(\mathbf{k}) = E(\mathbf{k})/\omega = (\omega/k)F(\mathbf{k})$. Note also that the saturation spectrum $B(\mathbf{k})$ (or the surface curvature spectrum) is expressed as $B(\mathbf{k}) = k^4\, F(\mathbf{k})$.

[18] The sources and sinks of energy $Q(\mathbf{k})$ consist of the wind forcing, viscous effects, dissipation via wave breaking, wave-wave interactions, and shorter wave generation by wave breaking, and can be written as

$$Q(\mathbf{k}) = \beta_\nu(\mathbf{k})\omega E(\mathbf{k}) - D(\mathbf{k}) - Q^{nl}(\mathbf{k}) + Q^{wb}(\mathbf{k}), \quad (16)$$

where $\beta_\nu(\mathbf{k}) = \beta(\mathbf{k}) - 4\nu k^2/\omega$ is the effective growth rate, which is the difference between the wind growth rate $\beta(\mathbf{k})$ and the rate of viscous dissipation (ν is the viscosity coefficient). Here the growth rate $\beta(\mathbf{k})$ is

$$\beta(\mathbf{k}) = C_\beta\left(u_*/c\right)^2\cos\varphi|\cos\varphi|, \quad (17)$$

where φ is the angle between wind and wave number vectors, u_* is air friction velocity, c is the phase velocity; C_β is a parameter corresponding to the parameterization by *Stewart* [1974] $C_\beta = 1.5(\rho_w/\rho_w)(\kappa^{-1}\ln(\pi/kz_0) - c/u_*)$, ρ_w, ρ_w are air and water density, $\kappa = 0.4$, and z_0 is roughness scale. The angular dependence in (17) results from the sheltering mechanism of wave generation, when the surface pressure acting on the downwind slope of short wave is proportional to the squared wind velocity component perpendicular to the wave crest. Thus short, slowly propagating surface waves aligned in the wind direction will grow, while they attenuate in the opposite direction.

[19] The rate of energy dissipation due to wave breaking $D(\mathbf{k})$ in (16) is [*Phillips*, 1985]

$$D(\mathbf{k}) = bg^{-1}c^5\Lambda(\mathbf{k}), \quad (18)$$

where b is an empirical constant of order 0.01, and $\Lambda(\mathbf{k})$ a statistical measure of wave breaking introduced by *Phillips* [1985], so that $\Lambda(\mathbf{k})d\mathbf{k}$ is the total length per unit area of the breaking front of surface waves in the wave number range from $\mathbf{k}$ to $\mathbf{k} + d\mathbf{k}$. The term $Q^{nl}(\mathbf{k})$ in (16) is the energy sink and source terms due to resonant four-wave (in gravity range) and three-wave (in capillary-gravity range) interactions.

[20] The source term $Q^{wb}(\mathbf{k}) = Q_{pc}^{wb}(\mathbf{k}) + Q_{sw}^{wb}(\mathbf{k})$ describes generation of short surface waves by wave breaking. Depending on the scale of a breaking wave, two mechanisms are specified. First, owing to the effect of the surface tension, short breaking waves with $k > k_{wb}$ (where $k_{wb} \approx 2\pi/0.3$ rad/m) are not disrupted, but produce "regular" trains of parasitic capillaries (bound waves). These parasitic capillaries provide energy losses in breaking waves. Therefore rate of generation of parasitic capillaries (described by term $Q_{pc}^{wb}(\mathbf{k})$) is proportional to the energy dissipation by the carrying short gravity wave at wave number $k_g = k_\gamma^2/k$, where $k_\gamma = (g/\gamma)^{1/2}$ is the wave number of minimum phase velocity. The description of this mechanism is given by *Kudryavtsev et al.* [1999, 2003a], and expression for $Q_{pc}^{wb}(\mathbf{k})$ reads

$$\begin{aligned} Q_{pc}^{wb}(\mathbf{k}) &\equiv \omega^3 k^{-5}I_{pc}(\mathbf{k}) \\ I_{pc}(\mathbf{k}) &= bk_g^{-1}\Lambda(\mathbf{k_g})\phi(k/k_\gamma) \end{aligned}, \quad (19)$$

where $I_{pc}(\mathbf{k})$ is dimensionless rate and $\phi(k/k_\gamma)$ is a filter function which restricts the action of source $I_{pc}(\mathbf{k})$ in k-space.

[21] The crests of longer breaking waves with wave number $k < k_{wb}$ that are disrupted result in mechanical perturbations of the sea surface. This mechanism is described in a recent paper by *Kudryavtsev and Johannessen* [2004]. It suggests that a breaking wave crest generates both subsurface turbulence and enhanced isotropic surface roughness with a totally saturated spectrum $F_{wb} \propto k^{-4}$ confined to the localized breaking zone [see, e.g., *Walker et al.*, 1996]. Once the wave crest has broken, localized enhanced roughness further disperses, feeding wave energy to areas away from the breaking zone. The short wave energy at a given point results from the total effect of wave breaking events randomly distributed over the surface. The rate of short wave (both gravity and capillary) generation $Q_{sw}^{wb}(\mathbf{k})$ is isotropic and proportional to F_{wb} multiplied by the frequency of wave breaking events per unit area. Expressing the latter quantity in terms of $\Lambda(\mathbf{k})$, the rate of short (gravity and capillary) wave energy generation by breaking waves is [*Kudryavtsev and Johannessen*, 2004]

$$\begin{aligned} Q_{sw}^{wb}(k) &\equiv \omega^3 k^{-5}I_{sw}(k) \\ I_{sw}(k) &= c_b\omega^{-1}\int_0^{k_m}\omega k^{-1}\Lambda(\mathbf{k})d\mathbf{k} \end{aligned}, \quad (20)$$

where I_{sw} is dimensionless rate, $c_b = 1.2 \cdot 10^{-2}$ is an empirical constant, and $k_m = \min(k/a_b, k_{wb})$ at $a_b = 10$ is the upper limit of integration defining interval of breaking waves which generate shorter waves at wave number k. As shown by *Kudryavtsev and Johannessen* [2004] in the capillary range, the efficiency of this mechanism is much weaker than generation of parasitic capillaries.

2.2.2. Short Wave Energy Source

[22] The form of the energy source (16) is quite complicated. However, in the equilibrium interval of the spectrum (far from the spectral peak), it may be significantly simplified. Here we adopt the same assumptions for Λ and Q^{nl} as discussed in the background model [Kudryavtsev et al., 2003a]. In that model, following Phillips [1985], it was suggested that in the equilibrium range the Λ-function (as well as D) can be parameterized as some power of saturation spectrum normalized on a threshold level α,

$$\Lambda(\mathbf{k}) = \frac{1}{2k}\left(\frac{B(\mathbf{k})}{\alpha}\right)^{n+1}. \qquad (21)$$

In the background model, four-wave resonant interactions were ignored while three-wave interactions (redistributing wave energy from the vicinity of minimum phase velocity toward lower and higher wave numbers) are assumed quadratic in wave spectrum: $Q^{nl} \propto \omega^3 k^{-5}B^2$. Then accounting for the parameterization (21), the energy source (16) combined with (18) reads

$$Q = \omega^3 k^{-5}\left[\beta_\nu(\mathbf{k})B(\mathbf{k}) - B(\mathbf{k})\left(\frac{B(\mathbf{k})}{\alpha}\right)^n + I_{sw}(k) + I_{pc}(\mathbf{k})\right]. \quad (22)$$

The second term in (22) parameterizes the nonlinear energy losses due to wave breaking (including generation of parasitic capillaries by microscale breaking) and three wave-interactions at $k/k_\gamma \propto 1$. Parameters α and n in (22) are functions of k/k_γ, which are equal to constants $\alpha = \alpha_g$, ($\alpha_g = 5 \times 10^{-3}$), $n = n_g$ ($n_g = 5$) at $k/k_\gamma \ll 1$, and equal to other constants (e.g., $n = 1$) in the vicinity of minimum phase velocity, at $k/k_\gamma \approx 1$. The third and fourth terms in (22) are dimensionless rate of short waves (free waves) and parasitic capillaries (bound waves) generation by wave breaking defined by (19) and (20). Details of definition of α and n functions are given by Kudryavtsev et al. [2003a]. Note also that if $I_{sw} = 0$ and $I_{pc} = 0$, (22) becomes similar to the spectral model proposed earlier by Donelan and Pierson [1987].

[23] At uniform conditions (no surface current and wind is steady) the shape of the equilibrium spectrum can be found as the solution of equation

$$Q[B(\mathbf{k})] = 0. \qquad (23)$$

This equation is easily solved numerically. However, below we shall use some approximate solutions, which are the following. In the range $k \leq k_\gamma$ (which is the most interesting for radar applications), term $I_{pc} = 0$. Aligned in the wind directions, the wave breaking source I_{sw} is small in comparison with direct wind energy input. Then the solution of (23) with (22) is

$$B_0(\mathbf{k}) = \alpha[\beta_\nu(\mathbf{k})]^{1/n}. \qquad (24)$$

This is considered as the reference spectrum. From (24) it follows that spectral energy vanishes in the azimuth plane where $\beta_\nu(\mathbf{k}) < 0$, in particular at cross-wind directions. In this vicinity (i.e., where $\beta_\nu(\mathbf{k}) \approx 0$) the wave spectrum is

$$B(\mathbf{k}) \approx \alpha\left[\frac{I_{sw}(k)}{\alpha}\right]^{\frac{1}{n+1}}. \qquad (25)$$

At the upwind directions where $\beta_\nu(\mathbf{k}) < 0$, one may anticipate low spectral density. Hence the nonlinear (second) term in (22) can be omitted, and the wave spectrum results from the balance of wave breaking source and energy losses due to viscosity and interaction with the opposing wind,

$$B(\mathbf{k}) \approx -\frac{I_{wb}(k)}{\beta_\nu(\mathbf{k})}. \qquad (26)$$

[24] The advantage of the wave breaking statistics proposed by Phillips [1985] is that the same $\Lambda(\mathbf{k})$-function defines both the energy dissipation (18), rate of short wave generation equations (19) and (20) (hence the shape of the spectrum), and fraction of the sea surface covered by breaking zones q needed for calculations of σ_0^p in (1),

$$q \propto \int_{k<k_{wb}^R} k^{-1}\Lambda(\mathbf{k})d\mathbf{k}, \qquad (27)$$

where $k_{wb}^R \approx \min(0.1k_r, k_{wb})$ is the wave number of the shortest breaking waves providing specular reflection of radio waves. In the equilibrium gravity range and at the background conditions, the energy input from wind is approximately compensated by energy losses by wave breaking. Thus the first and second terms in (22) are almost balanced, and using (21), the quantities q, I_{sw} and I_{pc} can be approximated by

$$q = c_q \int_\phi \int_{k<k_{wb}^R} \beta(\mathbf{k})B(\mathbf{k})d\varphi d\,\ln k, \qquad (28)$$

$$I_{sw}(k) = \frac{c_b}{2\alpha_g}\omega^{-1}\int\int_{k<k_m}\omega\beta(\mathbf{k})B(\mathbf{k})d\ln k d\varphi, \qquad (29)$$

$$I_{pc}(\mathbf{k}) = \beta(\mathbf{k_g})B(\mathbf{k_g})\phi(k_\gamma/k), \qquad (30)$$

where $c_q = 10.5$ is a constant chosen by Kudryavtsev et al. [2003a] to fit radar observations.

[25] Examples of the simulated short wave spectrum are shown in Figure 1. The dashed lines in Figure 1c show omnidirectional (integrated over φ) saturation spectra calculated from (23) for the energy source (22) where the wave breaking source $I_{sw}(k)$ is omitted. In this case the shape of the spectrum in the gravity and capillary-gravity range is governed by the wind forcing (first term in (22)), while in the capillary range it is governed by the generation of parasitic capillaries (term I_{pc}). Switching on the wave breaking energy source $I_{sw}(k)$ results in an increase of the spectral energy which is relatively small for the omnidirectional spectrum. However, the effect of wave breaking plays an important role in angular distribution of the wave energy. Angular distributions of $B(\mathbf{k})$ at typical radar wave numbers (P-, L-, C-, and Ku-bands) with and without the wave breaking energy source $I_{sw}(k)$ are shown in Figures 1b and 1a, respectively. The angular dependence of the folded spectrum defined as

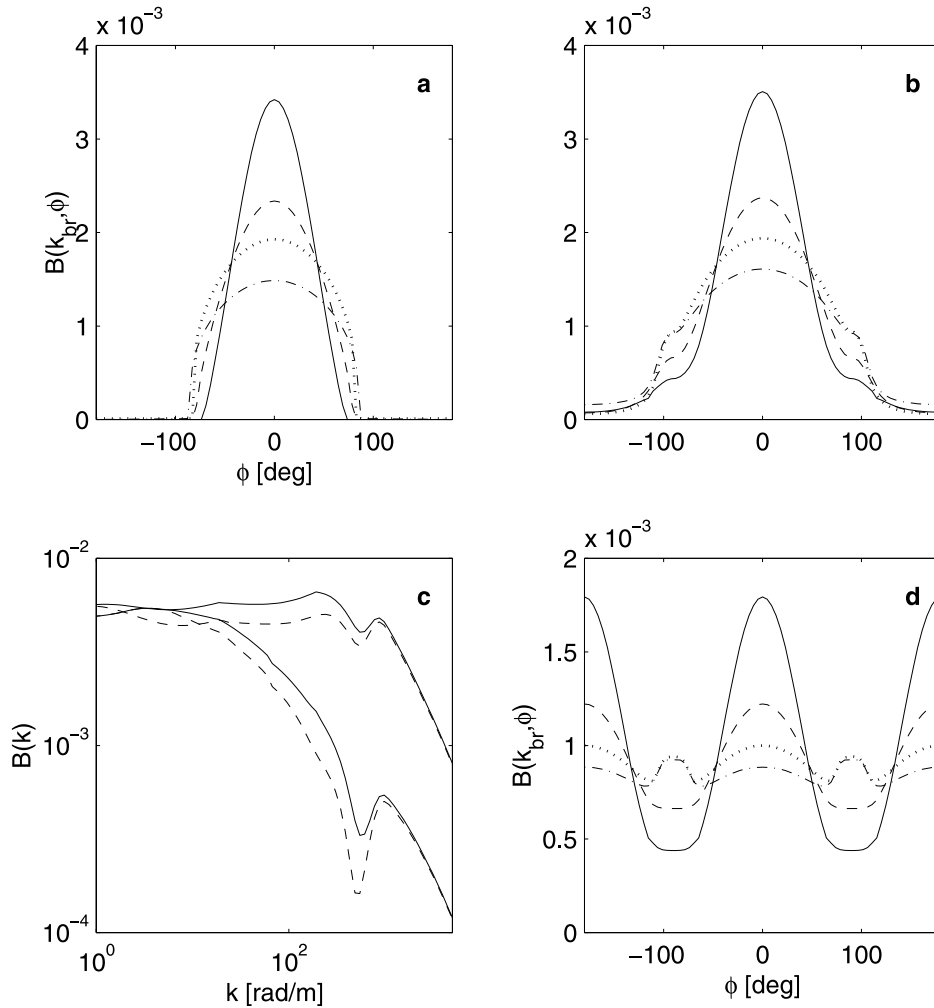$$B_r(\mathbf{k}) = 1/2 \cdot [B(\mathbf{k}) + B(-\mathbf{k})]$$

Figure 1. Model wave spectra. (a) Directional saturation spectra at wind speed 10 m/s for radar wave numbers corresponding to P-band (70 cm, dash-dotted line), L-band (21 cm, dotted line), C-band (5.6 cm, dashed line), and Ku-band (2.1 cm, solid line). Term I_{sw} (k) in (22) is omitted in reference calculations. (b) Directional saturation spectra, full model. The legend is the same as in Figure 1a. (c) Omnidirectional saturation spectra at wind speed 5 and 10 m/s (from down to up). Solid lines are the full model, dashed lines are reference calculations when term I_{sw} (k) in (22) is omitted. (d) Folded saturation spectra, full model. The legend is the same as in Figure 1a.

for the full model is shown in Figure 1d. The wave spectra calculated at $I_{sw}(k) \equiv 0$ are de facto described by (24). Since the wind forcing vanishes at cross-wind directions and becomes negative in the upwind directions, the wave spectral energy in the reference spectra (24) is restricted within that direction where **k** has a component aligned in the wind direction. Switching on the additional energy source $I_{sw}(k)$ due to breaking of longer waves feeds the energy to cross-wind and upwind directions, making the angular distribution of short wave spectra more realistic (see *Kudryavtsev and Johannessen* [2004] for discussion).

2.2.3. Spectral Peak

[26] In general, at the background conditions the shape of the spectral peak is also defined as the solution of (14), where only the second term (left-hand side) and first three terms for the energy source (22) are retained. However, the solution of this equation is quite difficult mainly due to Q^{nl} which is represented in the form of the "collision integral."

This problem is out of the scope of the present study. Following the background NRCS model the full wave number spectrum is defined as a composition of the equilibrium spectrum $B_{eq}(\mathbf{k})$ (defined as solution of (23) with (22)) and wave spectrum of energy-containing waves $B_p(\mathbf{k})$,

$$B(\mathbf{k}) = B_p\left(\mathbf{k}, \mathbf{u}_*/c_p\right) + B_{eq}(\mathbf{k}), \qquad (31)$$

where B_p is defined in the form proposed by *Donelan et al.* [1985] and restricted in $\vec{k}$-space as suggested by *Elfouhaily et al.* [1997]. In order to estimate q and I_{sw}, we need to define $\Lambda(\mathbf{k})$ for the energy-containing waves. Numerical solutions of (14) [see, e.g., *Komen et al.*, 1994] showed that the development of wave spectrum is almost provided by nonlinear energy transfer; that is, the advective term in the wave action conservation equation is approximately equal to Q^{nl}. In this case the wind energy input is balanced by the
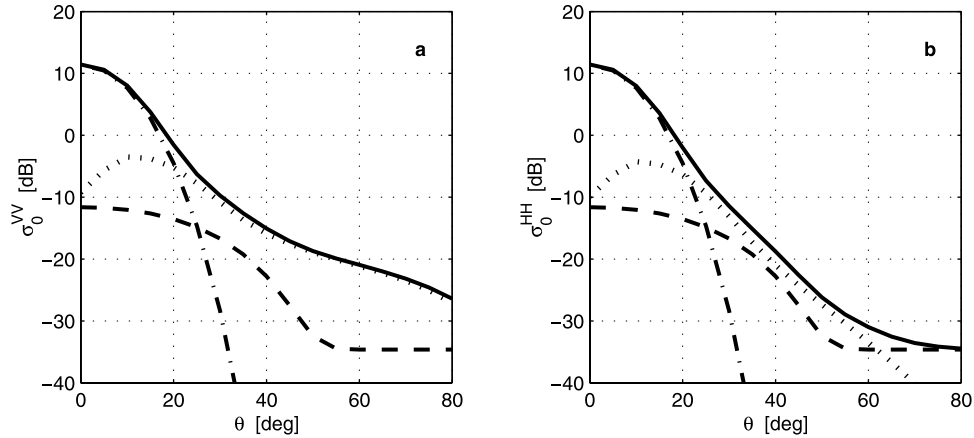
Figure 2. C-band NRCS as a function of incidence angle for (a) VV and (b) HH polarization at wind speed 10 m/s. Solid lines are the total NRCS (equation (1)). Dotted, dash-dotted, and dashed lines are contributions of Bragg scattering (second term in right-hand side of (2)), specular reflection (first term in right-hand side of (2)), and scattering from breaking waves (second term in (1)), correspondingly.

energy dissipation by wave breaking. Then from (18) the estimate of $\Lambda(\mathbf{k})$ reads

$$\Lambda(\mathbf{k}) \propto k^{-1}\beta(\mathbf{k})E(\mathbf{k}), \tag{32}$$

which has the same form as $\Lambda(\mathbf{k})$ in the equilibrium range. Thus the fraction of the sea surface covered by the breaking zone q and the wave breaking source I_{sw} (contributed by the full spectrum) are described by equations (28) and (29) where integration over k is expanded to the interval of energy-containing waves.

[27] In summary, we emphasize the dual effects of wave breaking on radio wave scattering, which play a crucial role in the radar imaging problem. First, breaking of waves with wave number $k < k_{wb}^R$ directly contributes to the NRCS by means of specular reflection from various surface patterns of breaking wave (that forms spike-like structure of radar signal). This contribution is described by the second term in (1) through the NRCS of individual breaking zone σ_{0b} (equation (12)) and fraction of the sea surface q (equation (28)) covered by breaking zones which will be large in comparison with radar wavelength. Quantity q is dependent on the radar wavelength (through the upper limit k_{wb}^R in the integral of equation (28)). For example, at wind speeds 5, 10, and 20 m/s the fraction of the sea surface contributing to specular reflection is respectively 0.25%, 2.03%, and 13.78% for Ku-band, and 0.03%, 0.21%, and 1.55% for L-band. Moreover, by assuming the same q at any moment (averaged over large surface area), the breaking waves appear on the sea surface stochastically. Wave breaking life span is much smaller than the period between the appearance of successive breaking events. Thus, once a wave is broken, it leaves localized disturbed surface, which disperses and feeds (along with wind forcing) the "regular surface" with the wave energy at a rate given by (29). The regular surface with fraction $1 - q$ provides radio wave scattering by means of Bragg scattering and specular reflection as described by the first term in (1) with (2). Breaking of short gravity waves (with wave number $k > k_{wb}$) generates trains of parasitic capillaries (with rate (30))

which provide Bragg scattering of radio waves at, for example, Ka-band.

2.3. Model Radar Scattering Properties

[28] Here we examine the results of the imaging model that combines the radar scattering model and the statistical properties of the sea surface resulting from solution of the energy balance equation for the background conditions (no current and steady wind).

[29] The dependence of the total NRCS (VV and HH) as well as its components, i.e., Bragg scattering, σ_{br}^p (second term in (2), Bragg spectrum and slope of tilting waves contribution), quasi-specular reflection, σ_{sp} (first term in (2); mean square slope contribution), and scattering from breaking waves, σ_{wb} (first term in (1)) on the incidence angle at a wind speed of 10 m/s is shown in Figure 2. At near-nadir incidence angles (less than 15°), quasi-specular reflection dominates the radar return for both VV and HH polarizations, while resonant Bragg scattering and scattering from wave breaking are negligible. Bragg scattering then gradually becomes the dominating source to the NRCS at moderate incidence angles from 20° to 30° for both VV and HH. In this region the impact of the composite scattering is similar to that obtained by *Voronovich and Zavorotny* [2001] from calculations of the integral equation written in the small slope approximation. In this incidence angle range the impact of wave breaking to the NRCS, although weak, is relatively more significant for HH polarization. This results from the fact that the σ_{wb} is independent of polarization and the Bragg scattering in HH polarization is less than in VV. For incidence angles larger than 30° (up to 60°) the Bragg scattering fully dominates at VV, while the Bragg scattering and scattering from wave breaking almost equally contribute to the NRCS at HH polarization.

[30] The relative contribution of breaking waves (σ_{wb}/σ_0^p), specular reflections (σ_{sp}/σ_0^p), and their sum ($\sigma_{wb} + \sigma_{sp})/\sigma_0^p$ (so-called non-Bragg scattering) to the total NRCS for C-band (top plots) and L-band (bottom plots) are shown in Figure 3. These quantities are presented as functions of the incidence angle at wind speed 10 m/s. Since σ_{wb} and σ_{sp} are independent of polarization and $\sigma_{br}^V > \sigma_{br}^H$, the relative
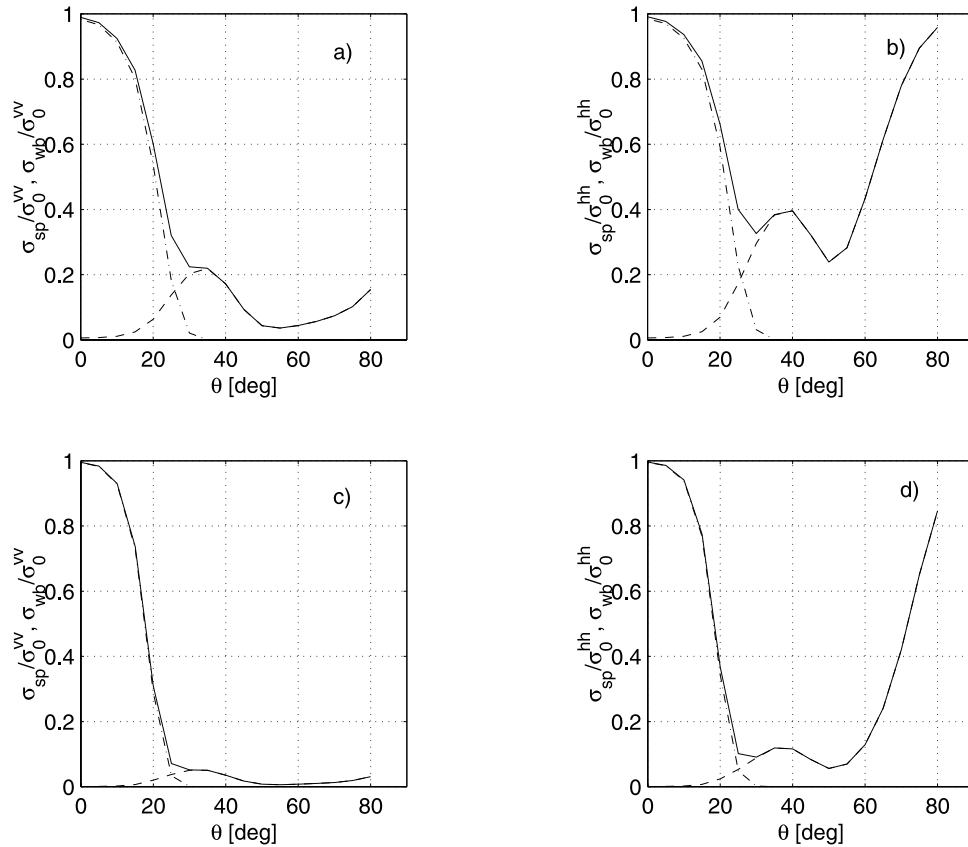
Figure 3. Relative contributions of quasi-specular reflection (dash-dotted lines), wave breaking (dashed lines), and their sum (solid lines) to the total NRCS at C-band ((a) VV and (b) HH polarizations) and L-band ((c) VV and (d) HH polarizations). Wind speed is 10 m/s.

contribution of non-Bragg scattering is higher in HH polarization than in VV. For C-band, quasi-specular reflections dominate the non-Bragg scattering (and total NRCS) at $\theta < 20°$. In contrast, wave breaking sufficiently contributes to the NRCS for both VV and HH at moderate incidence angles around $25°-40°$, but with dominating contribution in HH polarization. At larger incidence angles, on the other hand, the impact of wave breaking at VV decreases to a minimum around $50°$ followed by a slight increase, while a minimum is obtained for HH at around $50°$ followed by a rapid grow at larger incidence angles.

[31] For L-band (VV and HH polarization) the impact of non-Bragg scattering provides a different picture. First, as the range of waves providing specular reflection in L-band is narrower than at C-band, specular reflections dominate the NRCS only at incidence angles $\theta < 15°$. Second, the contribution of wave breaking is negligible at VV polarization for all incidence angles, while it seemingly plays an important role at grazing angles above $70°$ in HH polarization.

[32] An extensive comparison of the background NRCS model with observations is given by *Kudryavtsev et al.* [2003a]. In this section we therefore limit the comparison of the scattering properties to the newest findings addressed in sections 2.1 and 2.2. The modeled and empirically derived C-band [*Bentamy et al.*, 1994] and Ku-band [*Wentz and Smith*, 1999] NRCS of the sea surface for wind speed of 10 m/s are compared in Figure 4 as a function of incidence angles. Overall, the model is fairly consistent with the empirical results. In general, it gives the right functional

dependence on incidence angle although some underestimation of the NRCS in Ku-band is seen at large incidence angles. In the context of these results the most important feature of the radar scattering is polarization ratio ($P = \sigma_0^{VV}/\sigma_0^{HH}$) (equivalent to difference in dB) shown in Figure 4c. First of all, at small incidence angle the polarization difference is negligible because quasi-specular reflections dominate the sea surface NRCS. At incidence angles greater than about $20°$, on the other hand, the NSCAT model at Ku-band reveals a polarization difference that significantly deviates (about $3-5$ dB) from the "pure" Bragg scattering predictions (defined as a ratio of the scattering coefficient in (11): $|G^{VV}|^2/|G^{HH}|^2$). This is not a specific feature of the Ku-band, as it is also inherent to the C-band [e.g., *Vachon and Dobson*, 2000]. These deviations indicate the important role of the large-scale waves (with $k < k_d$) for the radar scattering. At moderate incidence angles the observed polarization difference is still around $2-3$ dB for the two-scale composite Bragg scattering model. This suggests that contribution of radar scattering from breaking waves is important. Finally, this is confirmed in the model calculations of the polarization difference for the total Bragg and non-Bragg scattering model leading to results that are consistent with the empirical data.

3. Transformation of Wind Waves

[33] The flowchart shown in Figure 5 schematically illustrates the radar scattering model described in sections 2.1 and 2.2. Bragg scattering (two-scale model), specular
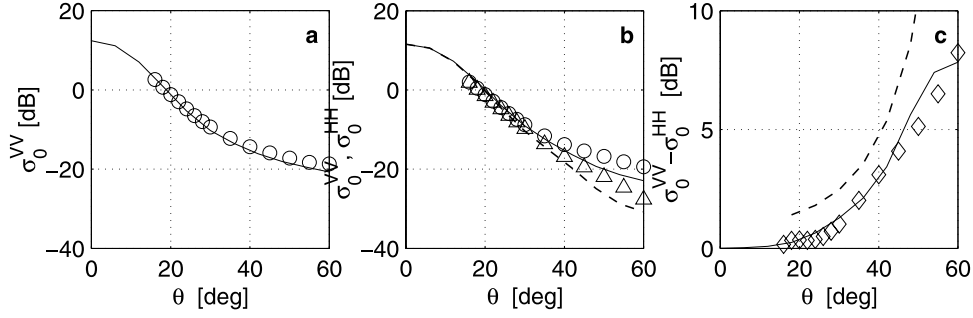
Figure 4. Comparison of the NRCS model (1) with empirical models at wind speed 10 m/s. (a) C-band: solid line is the model, circles are CMOD4 model [*Bentamy et al.*, 1994]. (b) Ku-band, VV (solid line and circles) and HH (dashed lines and triangles) polarizations. Lines are the model, and symbols are NSCAT model [*Wentz and Smith*, 1999]. (c) Ku-band: Polarization ratio. Solid line is the model, dashed line is the Bragg scattering model, and diamonds are NSCAT model.

reflections, and scattering from breaking waves are the three scattering mechanisms defining the NRCS of the sea surface provided its statistical properties are given. The spectrum of Bragg waves, the mean square slope of the sea surface, and fraction of the sea surface covered by wave breaking zones are the informative parameters of the sea surface, and their transformation in nonuniform medium results in radar manifestation of ocean features. We note that wave breaking not only contributes to the NRCS by means of specular reflections from breaking surface patterns (described by the second term in the right-hand side of (1)), but also generate additional (in respect to wind forcing) short waves which in turn contribute to the NRCS by means of Bragg scattering and specular reflections from "regular" surface (described by the first term in the right-hand side of (1)). Thus one may anticipate that wave breaking should play a significant role in the radar imaging formation.

[34] Description of the sea surface is based on the solution of the wave energy conservation equation. If the wind field is uniform and surface currents are absent, the solution of this equation describes the background sea surface. In case of a nonuniform medium, the same equation describes transformation of wind waves and thus radar informative parameters that determine the sea surface NRCS. We suggest that the sources of the medium nonuniformity are surface current, near-surface wind field, and surfactants. The transformation of wave action spectrum $N(\mathbf{k})$ in nonuniform medium is fully described by (14). To solve this equation, one needs to know the energy source Q. In the equilibrium range, Q is defined explicitly by (22). Unlike in the range of dominant waves, Q is not defined, and an empirical spectrum is specified instead. In this section we derive the equation for small disturbances of wave spectrum in the equilibrium range and in the range of dominant waves, and give its solution.

3.1. Energy Source in the Equilibrium Range

[35] We suggest that the wave spectrum, and thus the energy source in nonuniform medium, experiences small disturbances in respect to the background values. Then the variation in the source term (22) can be expressed as

$$\widetilde{Q} = \omega^3 k^{-5} \left[-\widetilde{B}/\tau + \widetilde{\beta} B + \widetilde{I}_{sw} + \widetilde{I}_{pc} \right], \quad (33)$$

where, hereinafter, a tilde denotes variation of any parameter in respect to the background value, and τ is the so-called dimensionless relaxation time defined here as

$$1/\tau(\mathbf{k}) = n\beta_\nu(\mathbf{k}) + (n+1)\lfloor I_{sw}(k) + I_{pc}(\mathbf{k})\rfloor/B(\mathbf{k}). \quad (34)$$

The second term in (33) describes the effect of wind surface stress variations on the wave spectrum, and terms $\widetilde{I}_{sw}$ and $\widetilde{I}_{pc}$ are variations in short wave energy sources due to the modulation by wave breaking,

$$\begin{aligned} \widetilde{I}_{sw}(k) &= \frac{c_b}{2\alpha_g}\omega^{-1}\left(n_g+1\right)\int\!\!\int_{k<k_m}\omega\beta B\frac{\widetilde{B}}{B}d\ln k d\varphi \\ \widetilde{I}_{pc}(\mathbf{k}) &= \left(n(k_g)+1\right)\frac{\widetilde{B}(\mathbf{k_g})}{B(\mathbf{k_g})}\beta(\mathbf{k_g})B(\mathbf{k_g})\phi \end{aligned} \quad (35)$$
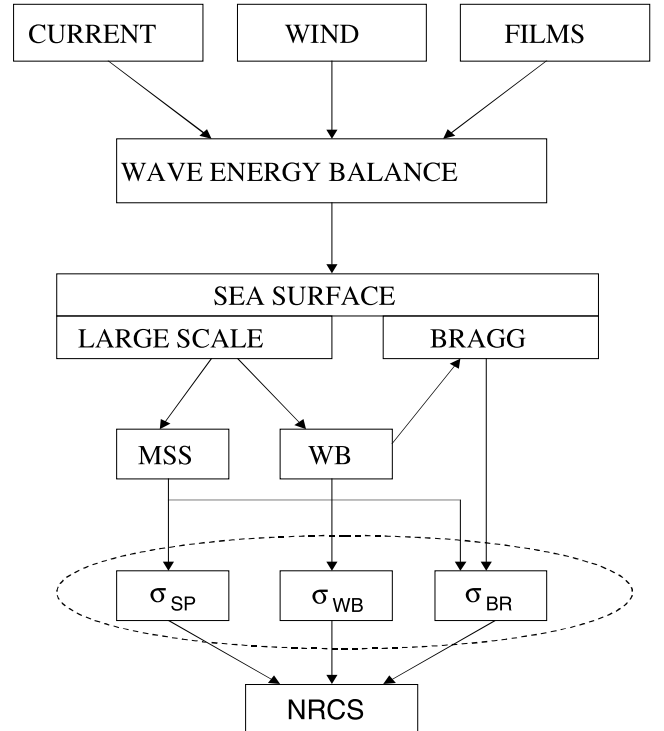

Figure 5. Schematic illustration of the radar imaging model structure.
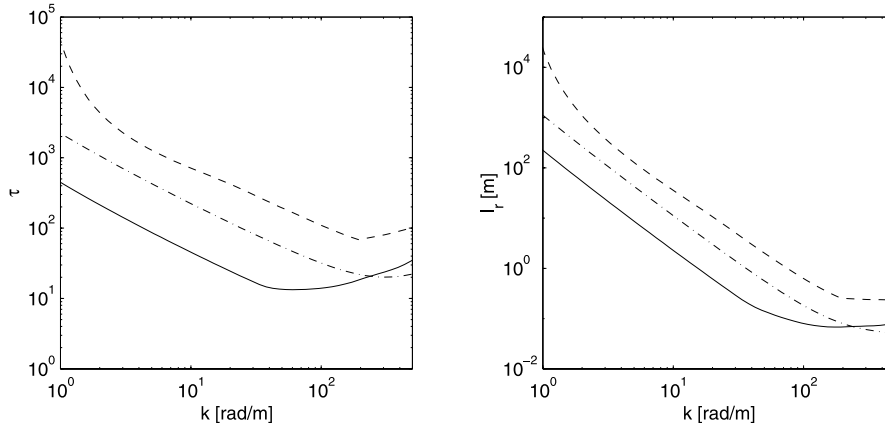
Figure 6. Dimensionless (left) relaxation time (42) and (right) relaxation scale $l_r = \tau \omega^{-1} c_g$ versus wave number at wind speed 10 m/s for downwind (solid lines), cross-wind (dashed lines), and upwind (dash-dotted lines) directions.

To obtain these equations from (19), (20) and (29), (30) we took into account that in the equilibrium gravity range, Λ is proportional to the saturation spectrum in power $(n + 1)$ (see (21)). Thus the relative variations in the wave breaking characteristics are $(n + 1)$-times amplified in comparison with relative spectral variations. We also suggest that in the range of energy-containing waves (where the explicit form of Λ is not known) the linear response of wave breaking on the small variation in wave spectrum has the same amplification factor.

[36] If the mechanism of short wave generation by breaking waves is not accounted for (terms $\widetilde{I}_{sw}$ and $\widetilde{I}_{pc}$ are omitted), (33) represents the energy source variation in a "standard" relaxation approximation, which is commonly used in the radar imaging problem. The dimensionless relaxation time (34) and corresponding relaxation scale $l_r = \tau c_g / \omega$ for downwind, cross-wind, and upwind directions at wind speed 10 m/s is shown in Figure 6. The relaxation parameter has a strong angular dependence with largest values in cross-wind directions. As discussed above, in downwind direction, the wave breaking source is small in comparison with the direct wind input; thus (34) can be simplified as $1/\tau \approx n\beta_\nu$. At cross wind the direct wind input vanishes; then (34) with (25) are reduced to $1/\tau \approx (n + 1)(I_{sw}/\alpha)^{n/(n + 1)}$. At upwind direction, (34) with (26) results in the following relaxation time $1/\tau \approx -\beta_\nu$. The range of τ change is thus an order of magnitude. Hence we may anticipate that short wave modulations by the current result in spatial isotropy of surface roughness.

3.2. Energy Source in Energy-Containing Waves

[37] Unlike the equilibrium range, in the range of energy-containing waves the source Q is not specified a priori, and the spectrum is defined empirically (spectrum B_p in (31)). In order to find variations in Q, we shall follow a relaxation time approach proposed by *Kudryavtsev* [1994]. An advantage of this approach is that the relaxation time τ is related to the shape of the spectrum, and thus is implicitly connected to the wave energy source, which is not known a priori. Field experiments carried out in the Gulf Stream frontal zone by *Kudryavtsev et al.* [1995] showed that model calculations of wave evolution based on the relaxa-

tion approach reproduce quite well the behavior of the dominant surface waves field in the current field.

[38] In the range of dominant waves, only the three first terms in (16) are retained. The expression for small variations in Q then reads

$$\widetilde{Q} = \widetilde{\beta}\omega E - \left(-\beta\omega + \frac{\partial}{\partial E}(D + Q^{nl})\right)\widetilde{E} \equiv \omega^3 k^{-5}\left[\widetilde{\beta}B - \widetilde{B}/\tau\right], \tag{36}$$

where

$$1/\tau = -\beta + \omega^{-1}\frac{\partial}{\partial E}(D + Q^{nl}) \tag{37}$$

is a dimensionless relaxation time for the dominant waves. To find τ, we note that the same (36) must describe spectral variations caused by either currents and/or wind. If the latter is a step-like disturbance of friction velocity δu_*, then for a large enough time $t(t \gg \omega^{-1}\tau)$ the wave spectrum reaches a new stationary state. As the variations in the wave spectrum, δN, need to satisfy $\widetilde{Q} = 0$, we obtain from (36)

$$\delta N/\tau = N\left(\partial\beta/\partial u_*\right)\delta u_*. \tag{38}$$

Since $\delta N = (\partial N/\partial u_*)\delta u_*$, (38) gives the following expression for the relaxation time:

$$1/\tau = \frac{2\beta(\mathbf{k})}{m_*}, \tag{39}$$

where $m_* = \partial(\ln N_0)/\partial \ln u_*$ is the wind exponent of the wave spectrum, and we have assumed that $\partial(\ln \beta)/\partial \ln u_* = 2$. Such a definition of τ does not require an exact form of Q, and one only needs to specify the spectral wind exponent, which may be known, for example, empirically.

[39] A shortcoming of this definition is that the relaxation time goes to infinite at cross wind, and becomes negative at opposite to the wind directions. This results from (17) for β and the fact that the empirical spectrum does not vanish (though it is small) at cross-wind and upwind angles. The

latter indicates that in the vicinity of the spectral peak, nonlinear wave-wave interactions (term Q^{nl}) are not a function but rather functional of the spectrum and spread of the energy away from the wind direction. Thus we may suggest that (17) is valid at that $\mathbf{k}$ which is aligned to the wind direction. On the other hand, at the opposite to the wind directions the effect of the wind is the only energy sink. Following an analogy with the equilibrium range, we suggest that the relaxation time at upwind direction is $1/\tau = -\beta$. Thus in order to avoid both infinite and negative relaxation time, we merge these two asymptotes. The estimate of τ at arbitrary angle is thus

$$1/\tau_p = \max\left(2\beta(k, \varphi)/m_*, \beta(k, 0^0)\right). \qquad (40)$$

In the range of energy-containing waves the spectral level is $B \propto (u_*/c_p)^{0.55} (k/k_p)^{1/2}$, where the spectral peak wave phase velocity c_p and wave number k_p are functions of dimensionless fetch $\hat{x} = Xg/u_*^2$, $u_*/c_p = f(\hat{x}) \propto \hat{x}^{-0.33}$ [Donelan et al., 1985]. Then for a given fetch X the spectral wind exponent in the range of energy-containing waves is

$$m_* = 1 + 0.9\partial \ln f / \partial \ln \hat{x}. \qquad (41)$$

For the fully developed sea, $\partial(\ln f)/\partial(\ln \hat{x})$ is zero, while for the young sea it is $\partial(\ln f)/\partial(\ln \hat{x}) = -0.33$. Thus the wind exponent for developed seas is $m_*^p = 1$, which indicates that the dominant role in the nonlinear energy source is by resonant wave-wave interactions (which are cubic in spectrum). In developing spectrum, $m_*^p \approx 0.7$, which in turn indicates that both wave-wave interactions and wave breaking are equivalent.

[40] As already emphasized, $\widetilde{I}_{pc}$ and $\widetilde{I}_{sw}$ vanish in the range of energy-containing waves. Thus the energy source (33) will be valid in the full wave number range if τ^{-1} is a combination of the relaxation time τ_{eq} in the equilibrium range (equation (34)) and τ_p in the dominant wave range (equation (40)). By taking into account the spectral model (31), we can express τ^{-1} as

$$1/\tau = (B_p/\tau_p + B_{eq}/\tau_{eq})/B. \qquad (42)$$

Thus (33) with (42) describes the energy source in the full wave number range.

3.3. Wave Spectrum Modulation

[41] Let us assume that the surface current and wind velocity may be expanded into the Fourier series

$$z(\mathbf{x}, t) = \int \hat{z}(\mathbf{K}) \exp(i(\mathbf{K} \cdot \mathbf{x} - \Omega t)) d\mathbf{K}, \qquad (43)$$

where $z(\mathbf{x},t)$ is an arbitrary quantity, $\hat{z}(\mathbf{K})$ is its Fourier amplitude (complex variable), and $\mathbf{K}$ and Ω are wave number vector and frequency. Note that only the real part of equation (43) has a physical meaning. Then solution of the linearized equation (14) with (33) and (42) in terms of Fourier harmonics for the small spectrum modulations induced by surface current and near-surface wind reads

$$T(\mathbf{k}, \mathbf{K}) = \frac{\tau}{1 + i \cdot r}\left[\omega^{-1} m_k^{ij}\hat{u}_{i,j} + \hat{\beta} + (\hat{I}_{sw} + \hat{I}_{pc})/B\right], \qquad (44)$$

where $T(\mathbf{k}) = \hat{N}(\mathbf{k})/N_0(\mathbf{k})$ is the transfer function, r is the dimensionless relaxation parameter

$$r = \tau\omega^{-1}(c_{gj}K_j - \Omega), \qquad (45)$$

$m_k^{ij} = k_j\partial \ln N_0/\partial k_i$ is a tensor of the "wave number exponent" of the spectrum, and $\hat{u}_{i,j}$ is the Fourier amplitude of current velocity gradient tensor $\partial u_i/\partial x_j$. The operator $m_k^{ij}\hat{u}_{i,j}$ in (44) is

$$m_k^{ij}\hat{u}_{i,j} = m_k\left(\cos^2 \varphi \cdot \hat{u}_{j,j} - \cos 2\varphi \cdot \hat{u}_{2,2}\right) + 1/2m_\varphi \sin 2\varphi$$
$$\cdot (\hat{u}_{2,2} - \hat{u}_{1,1}) + 1/2m_k \sin 2\varphi \cdot (\hat{u}_{2,1} + \hat{u}_{1,2})$$
$$- m_\varphi\left(\sin^2 \varphi \cdot \hat{u}_{2,1} - \cos^2 \varphi \cdot \hat{u}_{1,2}\right), \qquad (46)$$

where φ is the direction of the wave number vector, $m_k = \partial \ln N/\partial \ln k$, and $m_\varphi = \partial \ln N/\partial\varphi$. Terms $\hat{I}_{sw}$ and $\hat{I}_{pc}$ in (44) describe the effect of wave breaking modulations on the short wind and parasitic capillary waves. Expressions for these terms are given by (35) where the spectral variations $\widetilde{B}/B$ in physical space are replaced by the transfer function $T(\mathbf{k})$. The second term in (44) describes effects of the wind on the wave modulations. In particular, wind variations can result from the atmospheric boundary layer transformation over the sea surface temperature front. In this case atmospheric stratification causes varying surface wind stress (friction velocity) affecting β and hence wind waves via $\hat{\beta} = 2\beta\hat{u}_*/u_*$. Note that (44) also describes the short wave modulation by long surface waves considered, for example, by Kudryavtsev et al. [2003b]. In this case one needs to assume that $\Omega/(Kc_g) \gg 1$ and $\widehat{u}_{1,1} = iAK\Omega$ (A is amplitude of surface wave traveling along x_1 axis).

[42] Notice that effect of surfactants has not been included in (44) explicitly. Surfactants may significantly affect the coefficient of viscous dissipation, and thus they affect the wave spectrum via the effective growth rate β_ν in (16) [e.g., Ermakov et al., 1992]. This mechanism is local in k-space, and mainly influences the shortest wind waves whose relaxation rate is very fast (see Figure 4). Thus we may suggest that surfactants affect short waves locally in the physical space and can be accounted for through modified viscosity coefficient in the background spectrum $N_0(\mathbf{k})$. Hence the variation of the wave saturation spectrum in the physical space is

$$B(\mathbf{k}) = B_0(\mathbf{k})\left[1 + \int T(\mathbf{k}, \mathbf{K})e^{i(\mathbf{K}\cdot\mathbf{x} - \Omega t)}d\mathbf{K}\right], \qquad (47)$$

where the effect of wind and surface current are included in $T(\mathbf{k})$ (according to (44)) and the effect of surfactants is included in $B_0(\mathbf{k})$ (through solution of (23) with (22)).

[43] Equation (44) represents the Fredholm Integral Equation of the Second Kind. Such an equation can be solved numerically by iterations. However, first we consider some limited cases (for stationary currents, $\Omega = 0$) which illustrate some characteristic properties of the full solution.

[44] In the case where parameter r is large, the spatial scale of surface changes is small in comparison with relaxation scale l_r. This is most plausible for long gravity waves. At $r \gg 1$, (44) reduces to

$$T(\mathbf{k}, \mathbf{K}) = \frac{m_k^{ij}K_j\hat{u}_i}{c_{gj}K_j} \propto -\frac{7}{2}\frac{V}{c_g}, \qquad (48)$$

where V is the magnitude of the surface current. This represents transformation when the surface waves interact

with the current as free waves and do not feel the impact of wind or other energy source. In this case the faster (and longer) the surface waves, the smaller is the effect of the surface current. It can be shown that the second and third terms in (44) have the order $r^{-1}\hat{u}_*/u_*$ and $r^{-1}V/c_g$, respectively, and can thus be omitted at $r \gg 1$.

[45] The condition where parameter r is small ($r \ll 1$) is fulfilled for short wind waves. Here the effect of the current is negligible (first term in (44) can be omitted), and the spectrum variations result from the local impact of wind and wave breaking. When the wind is the only source of short waves variability, (44) is reduced to

$$T(\mathbf{k}) \approx m_* \frac{\hat{u}_*}{u_*}, \qquad (49)$$

where m_* is the spectral wind exponent. Thus variations in wave spectrum reflect spatial nonuniformity of surface wind stress. If the wind is uniform, the only source of short wave modulations is breaking of larger waves. Assuming that the transfer function for breaking waves is $T \approx m_k^{ij}\hat{u}_{i,j}\omega^{-1}\tau$, the short wave modulation transfer function can be written as

$$T(\mathbf{k}) \approx m_k \frac{n_g+1}{n_g} \ln\left[\frac{k}{a_b k_p}\right]\tau\omega^{-1}\hat{u}_{j,j}, \qquad (50)$$

where $a_b = 10$ is a constant in (20). To derive this equation we take into account that only the first term in the operator in (46) contributes to the integral over φ. Equation (50) contains two remarkable features: (1) Only the divergence of the surface current affects short wind wave modulations, and (2) the modulation is strongest at cross-wind directions (due to angular behavior of τ). The latter suggests that the effect of the surface current results in anisotropy of short wind waves.

[46] This important result can be illustrated by calculations of the transfer function $|T(\mathbf{k})|$ for a "pure" divergent current

$$u_1 = u_m \exp[iK(x_1 - Ct)] \qquad (51)$$

and a "pure" shear current

$$u_2 = u_m \exp(iKx_1) \qquad (52)$$

as shown in Figure 7 for the airflow directed along the x_1 axis. The transfer function for the "standard" relaxation solution (terms $\hat{I}_{sw}$, $\hat{I}_{pc}$ in (44) are omitted) is shown in Figure 7a, while the full transfer function is shown in Figure 7b. The spectral behavior of the standard $|T(\mathbf{k})|$ is defined by the first factor in (44). It decreases toward very short wind waves (since relaxation scale $l_r K \ll 0$), and toward the longest wind waves. The latter results from approximation of (48). At $U_{10} = 5$ m/s and for the waves traveling in the wind direction the maximum of $|T|$ locates in the range of meter-wavelength, while for the wave opposing the wind it is in the range of decimeter-wavelength. This is a consequence of the relaxation time that increases with increasing deviation of the wave and wind directions. Switching on of the wave breaking source in (44) completely changes the spectral behavior of $T(\mathbf{k})$. Wave breaking significantly increases the amplitude of the transfer function, especially in the range of short waves, where the effect of direct interaction with the current (straining effect) is weak. As was discussed above (see (50)) the impact of wave breaking on short wave modulations

increases with increasing deviation of the wave number vector from the wind direction. If convergent current has a velocity of advance (case of internal waves, $C \neq 0$), shape of the transfer function is changed; see Figure 7d. In the low-frequency part of the spectrum a new peculiarity in $|T(\mathbf{k})|$ has appeared. It is expressed as a local maximum around the resonant curve $c_g \cos \varphi = C$, where the relaxation parameter r is zero. Enhancement of wave spectrum in low-frequency range stimulates wave breaking which in turn affects short wave modulations. That is why the transfer function in the range of short waves is increased in comparison with the case of $C = 0$. Figure 7c shows transfer function for the "pure" shear current in (52). For the considered conditions (wind is directed along x_1-axis) the maximum of the transfer function (as it follows from operator (46)) should appear in the azimuth plane which is close to $\pi/2$, and $|T(\mathbf{k})|$ should be larger the narrower angular distribution of wave spectrum. In the short wave range this effect disappears due to small relaxation time. Comparing the shape of the transfer function for divergent current (Figure 7b) with that for and shear current (Figure 7c), one may mention that in the latter case the effect of wave breaking for the short wave modulations is not observed. This surprising (at first glance) result is a simple consequence of the fact that $\hat{I}_{sw}$ in (44) vanishes because the integral of $T(\mathbf{k})$ for breaking waves (which is the odd function of φ) over all directions is zero.

[47] The above-mentioned peculiarities are well-expressed in amplitudes of omnidirectional spectrum modulations shown in Figure 8. For convergent current the standard relaxation solution exhibits pronounced response in low-frequency intervals and suppression of wave modulations in short wave ranges. Comparing Figures 8a and 8b, one may observe that resonance between moving current and wind waves results in much stronger modulations in the vicinity of resonant wave number $k \approx g/(4C^2)$. Switching on the effect of wave breaking generates modulations in short waves, in particular at wave numbers related to L-, C-, and X-bands. Comparing solid and dashed lines in Figure 8, we arrive at the conclusion that wave breaking significantly affects wind wave modulations.

[48] In the case of shear current, modulation of the omnidirectional spectrum vanishes for both the standard relaxation solution and the full one. This is a consequence of the fact that operator (46) at chosen wind direction is the odd function of φ, and vanishes after integration over all directions.

3.4. Transformation of the Mean Square Slope and Wave Breaking

[49] To calculate the total NRCS we need to quantify the mean square slope and the amount of wave breaking. Using the spectral transfer function (44), the variations of the components of the mean square slope Δs_j^2 in a nonuniform medium reads

$$s_j^2 = s_{j0}^2 \left(1 + \Delta s_j^2/s_{j0}^2\right),$$

$$\Delta s_j^2 = \int T_j^s(\mathbf{K}) e^{i(\mathbf{K}\cdot\mathbf{x} - \Omega t)} d\mathbf{K}, \qquad (53)$$

$$T_j^s(\mathbf{K}) = \int\limits_{k<k_d} \int T(\mathbf{k},\mathbf{K})\kappa_j^2 B(\mathbf{k}) d\varphi d\ln k,$$
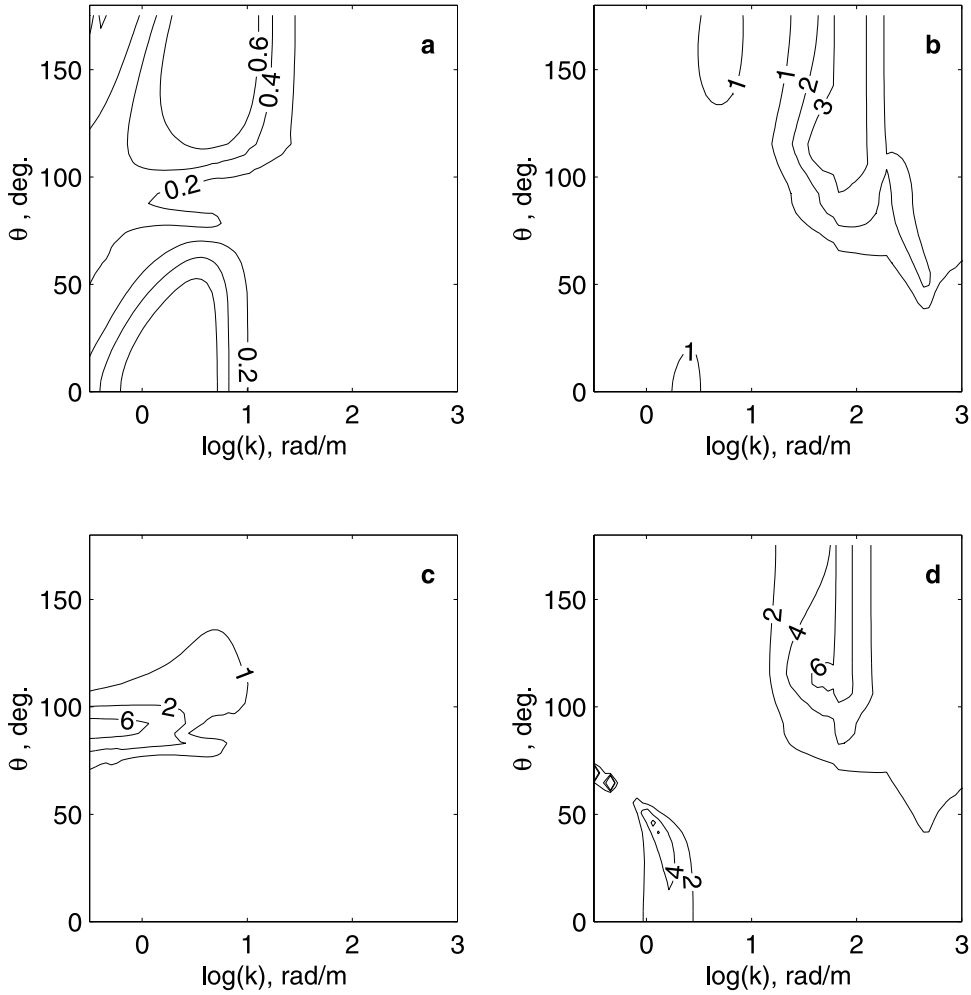
Figure 7. Amplitude of wave spectrum variations at wind velocity 5 m/s directed along the x_1 axis for the model currents. Current velocity amplitude is $\hat{u} = 0.25$ m/s, and wave number is $K = 2\pi/1000$ rad/m. (a) "Standard" relaxation approach; only the first term in $T(\mathbf{k})$ is retained. Case is of divergent current (51) with C = 0. (b) Full model, divergent current (51) with C = 0. (c) Full model, shear current (52). (d) Full model, divergent current (51) with $C = 1$ m/s.

where the subscript "0" indicates that the mean square slope corresponds to the background spectrum $B_0(\mathbf{k})$ in (47), $\kappa_j = k_j/k$ is the unit wave number vector, and subscript "j" is $j = 1,2$.

[50] Equation (28) defines the fraction of the sea surface covered by wave breaking zones. The length of wave breaking crests, Λ (which defines q according to (27)) is a strong nonlinear function of the saturation spectrum. Thus, as discussed above (see (35)), its small variations result in strong variations of q which are amplified by $(n_g + 1)$ in comparison with the spectrum variations. Then the fraction of the sea surface covered by breaking zones is

$$q = q_0(1 + \Delta q/q_0),$$

$$\Delta q = \int T^q(\mathbf{K})e^{i(\mathbf{K}\cdot\mathbf{x} - \Omega t)}d\mathbf{K},$$

$$T^q(\mathbf{K}) = (n_g + 1)\int_{k<k_{wb}^R}\int T(\mathbf{k}, \mathbf{K})\beta B(\mathbf{k})d\varphi d\ln k,$$
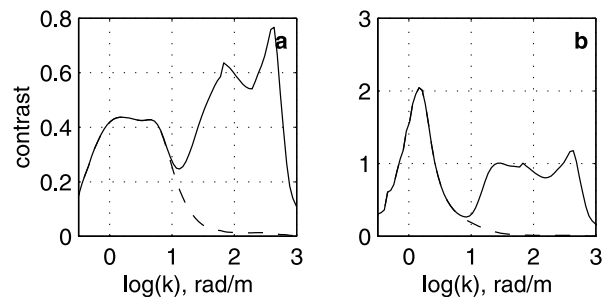
(54)

Figure 8. Amplitude of omnidirectional spectrum modulations for the convergent current (51) at (a) C = 0 and at (b) C = 1 m/s. Current velocity amplitude is $\hat{u} = 0.25$ m/s, and wave number is $K = 2\pi/1000$ rad/m. Dashed lines show calculations on "standard" relaxation solution, when only first term in $T(\mathbf{k})$ of (44) is retained. Solid lines show full solution when effect of wave breaking is accounted for.

where (we remind that) the upper limit of integration is related to the radar wave number as $k_{wb}^R = \min(k_{wb}, 0.1k_r)$.

4. Role of the Atmospheric Boundary Layer and Surfactants

4.1. Marine Atmospheric Boundary Layer (MABL)

[51] The influence of the marine atmospheric boundary layer (MABL) on wind waves and thus radar scattering comes through the local friction velocity defining the background wave spectrum and the second term in (44) describing an adjustment of wind waves to varying wind stress. Changes in the air and the sea surface temperatures can alter the stratification in the MABL and subsequently the boundary layer turbulence and near-surface wind stress. Here we consider only the impact of the sea surface temperature on the radar scattering.

[52] Ocean current features are usually accompanied with spatial variations of the sea surface temperature T_w (temperature fronts). Field experiments by *Kudryavtsev et al.* [1996] showed that changes in the vertical shear of wind velocity and air temperature at height of the measurements were well correlated with the spatial changes of the ocean surface temperature. Coincident shipborne radar measurements revealed stronger radar scattering from the locally warm surface areas and a decrease from the locally colder surface areas. *Beal et al.* [1997] reported on similar depression of the radar returns on the cold side of the Gulf Stream front and enhancement on its warm side.

[53] To assess the effect of changes in MABL stratification on radar images, we assume that the geostrophic wind speed and temperature of the free atmosphere (at the height comparable with the planetary MABL depth, which is of order 1 km) are horizontally uniform. Then any variations in the near-surface wind field are the result of the planetary MABL transformation over the spatially varying sea surface temperature (SST). Such SST variations are typically step-like across a temperature front. The corresponding adjustment of the MABL to this SST change occurs within an internal boundary layer (IBL) which is developing on the downwind side of the sea front. The depth of the IBL δ increases away from the front, and at a distance of order $X \propto G/f$ (G is geostrophic wind speed, f is the Coriolis parameter) it attains the thickness of a new equilibrium planetary MABL fully adjusted to a "new" SST. The description of the stratified IBL evolution is quite a complicated problem and is not in the scope of the present study (a review on the IBL studies is given, for example, by *Venkatram* [1977]).

[54] In the following we seek a realistic estimate of the surface wind stress variation over a SST front. At the distance exceeding $X_0 \propto 10^{-2} G/f$ the IBL develops inside the Ekman part of the MABL, where vertical changes of wind velocity are small. In this case we may assume that the momentum and heat fluxes are insensitive to the stage of IBL development and close to the fluxes which are typical for the equilibrium MABL on the downwind side of a front. Thus we suggest that at each point across the temperature front the surface wind stress may be estimated through the resistance law for the equilibrium planetary MABL [e.g., *Zilitinkevich*, 1970; *Brown*, 1982],

$$\frac{\kappa \mathbf{G}}{\mathbf{u}_*} = \ln\left(\kappa u_*/fz_0\right) - B(\mu) - iA(\mu), \tag{55}$$

where $\mu = \kappa u_*/fL$ is the stratification parameter of the planetary MABL, $L = -u_*^3/(\kappa \beta_a Q_S)$ is the Monin-Obukhov scale, β_a is the buoyancy parameter, Q_S is the surface kinematics heat flux, $\mathbf{G} = G \exp(i\varphi_G)$ is the complex geostrophic wind velocity with direction φ_G, $\mathbf{u}_* = u_* \exp(i\varphi_w)$ is the complex friction velocity at the sea surface, φ_w is the direction of the near-surface wind, z_0 is the sea surface roughness scale, and $A(\mu)$, $B(\mu)$ are universal dimensionless function for the planetary MABL. For practical reasons the stratification parameter can be estimated through a "bulk" equation

$$\mu = \kappa^2(g/T_{aK})(T_a - T_w)/fG, \tag{56}$$

where $\kappa = 0.4$ is the Von Karman constant, T_a is the potential temperature at the upper boundary of the planetary MABL (that corresponds to the potential temperature of the free atmosphere on the height of order 1 km), and T_{aK} is the T_a in $°K$. Equation (56) follows from the definition of the stratification parameter $\mu = \kappa u_*/fL \equiv \kappa^2 \beta \theta_*/(fu_*)$ (where $\theta_* = -Q_0/u_*$ is the air temperature scale), and the assumption that the square root ratio of the heat to momentum transfer coefficients is close to unit, i.e., $(C_H/C_D)^{1/2} \approx 1$.

[55] The universal function may be defined either empirically [e.g., *Zilitinkevich*, 1970] or theoretically. When a simplified two-layer model of the planetary MABL is chosen [*Brown*, 1982] the universal dimensional functions $A(\mu)$ and $B(\mu)$ satisfy the equations

$$A(\mu) = \Phi(\varepsilon\mu A(\mu))/(2\varepsilon)$$
$$B(\mu) = -A(\mu) + \Psi(\varepsilon\mu/A(\mu)) - \ln(\varepsilon/A(\mu)), \tag{57}$$

where $\varepsilon = 0.15$ and $\Phi(x)$ and $\Psi(x)$ are universal functions of the Monin-Obukhov similarity theory respectively defining wind shear and wind velocity profile.

[56] Equations (55) and (56) give the friction velocity at the sea surface in the MABL adjusted to the SST changes across the front. The geostrophic drag coefficient

$$C_D = u_*^2/G^2 \tag{58}$$

as a function of the temperature difference $T_a - T_w$ is plotted in Figure 9a for geostrophic wind speeds of 5 and 15 m/s. Assuming that the MABL stratification on the upwind side of a SST front is neutral ($T_a - T_w = 0$), and that the airflow runs from the warm to the cold (or from cold to the warm) side with the surface temperature drop $|\Delta T_w| = 5°C$, the surface wind stress on the downwind side is decreased (or increased) by a factor of 2. Such a decrease/increase of the wind stress may cause significant variations in short wind waves and thus in radar backscatter power over the SST front.

[57] The linear response of the friction velocity to the surface temperature variation $\widetilde{T}_w$ is given by

$$\frac{\widetilde{u}_*}{u_*} = \left[\frac{1}{2C_D}\frac{\partial C_D}{\partial T_w}\right]\widetilde{T}_w. \tag{59}$$

The transfer function $1/2\partial(\ln C_D)/\partial T_w$ as a function of the air-sea surface temperature difference for geostrophic wind speeds 5m/s and 15m/s is plotted in Figure 9b. As expected,
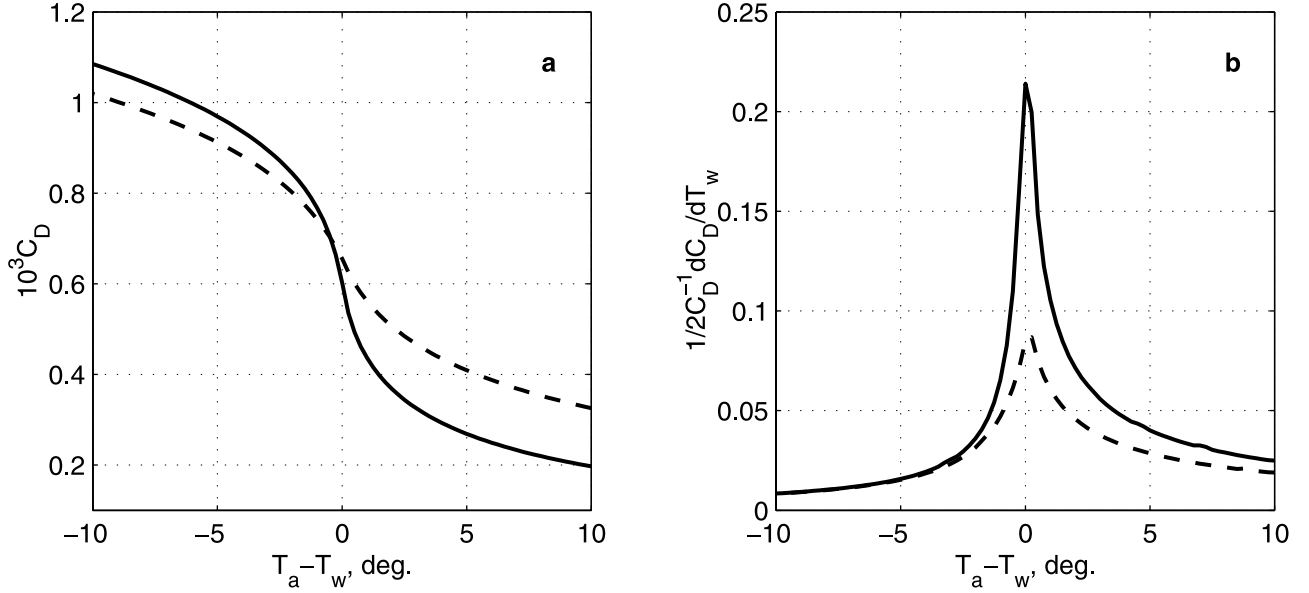
Figure 9. (a) Geostrophic drag coefficient as a function of the temperature drop between the sea surface and free atmosphere for geostrophic wind speed 5 m/s (solid line) and 15 m/s (dashed line). (b) Corresponding transfer function $1/2\partial(\ln C_D)/\partial T_w$ describing the linear response of air friction velocity on the surface temperature variations according to (59).

the response of friction velocity to surface temperature variation is strongest when they occur relative to a neutrally stratified MABL, while the response is weak if the background stratification is either strongly stable or unstable. Moreover, the response of the friction velocity decreases with increasing geostrophic wind speed. These features of the transfer function are a consequence of the behavior of C_D on $(T_a - T_w)$ and G as shown in Figure 9a. These calculations can in turn be used to estimate the NRCS difference $\Delta\sigma_0^P$ over a SST front. If the NRCS is $\ln(\sigma_0^P) \propto m_*^P \ln(u_*)$ (m_*^P is wind exponent of the NRCS), then

$$\frac{\Delta\sigma_0^P}{\sigma_0^P} \approx m_*^P \left[\frac{1}{2C_D} \frac{\partial C_D}{\partial T_w} \right] \Delta T_w.$$

Thus the data shown in Figure 9b multiplied by m_*^P give an estimate of the NRCS drop over a front. Although this is a linear estimate, it confirms experimental findings that spatial changes in the SST associated with oceanic fronts are visible in radar images at low to moderate wind speeds.

4.2. Impact of Surfactants

[58] It is a well-known fact that surface films suppress short wind waves [e.g., *Johannessen et al.*, 1997; *Espedal et al.*, 1998; *Ermakov et al.*, 1992]. Surfactants of natural or artificial origin always exist on the sea surface. They are transported by the currents and accumulated in the zones of current convergence. Hence suppression of short wind waves in narrow convergence zones can be used to trace the wind-driven current (by means of wind streaks resulting from Langmuir circulation), mesoscale current variability, and internal waves [e.g., *Espedal et al.*, 1998; *da Silva et al.*, 1998].

[59] Suppression of short wind waves results from a strong increase of the molecular viscous dissipation. It is

explicitly included in the wave spectrum model (through the effective growth rate $\beta_\nu(\mathbf{k})$ in (16)). Thus to account for the effect of surfactants, we need an expression relating effective molecular viscosity ν_{ef} to surfactants properties. In the case of the monomolecular films the effective viscosity coefficient is defined as [*Levich*, 1962]

$$\nu_{ef} = \nu \frac{1 - \frac{E_f k^2}{\rho\sqrt{2\nu\omega^3}} + \frac{E_f^2 k^3}{4\rho^2\sqrt{2\nu^3\omega^5}}}{1 - \frac{2E_f k^2}{\rho\sqrt{2\nu\omega^3}} + \frac{E_f^2 k^4}{\rho^2\nu\omega^3}},$$

where ν_{ef} and ν are the molecular viscosity coefficient in the presence of film and for clean surface, respectively, and E_f is a surface film elasticity module.

[60] Figure 10 illustrates the model effect of the surface film on the short wind wave spectrum at wind speed of 5 and 15 m/s. In these calculations a film elasticity is specified as 5, 10, and 20 mN/m. As anticipated, the effect of surfactants is strongest for the shortest waves. However, down in the capillary range the effect becomes less pronounced than in the vicinity of capillary-gravity waves. This explains the mechanism of generation of parasitic capillaries, which receive energy from short gravity waves and thus partially restrains enhanced viscous dissipation. At a given elasticity the spectral contrast decreases with increasing wind speed. At a wind speed of 5 m/s the C-band Bragg waves can be totally suppressed by surface film, while at higher winds the effect of surface film (even maximum elasticity) is very weak.

5. Comparison With Measurements

[61] In this section the model simulations are compared to radar signatures of internal waves (IW) obtained during the JOWIP [*Hughes and Dawson*, 1988] and the SARSEX
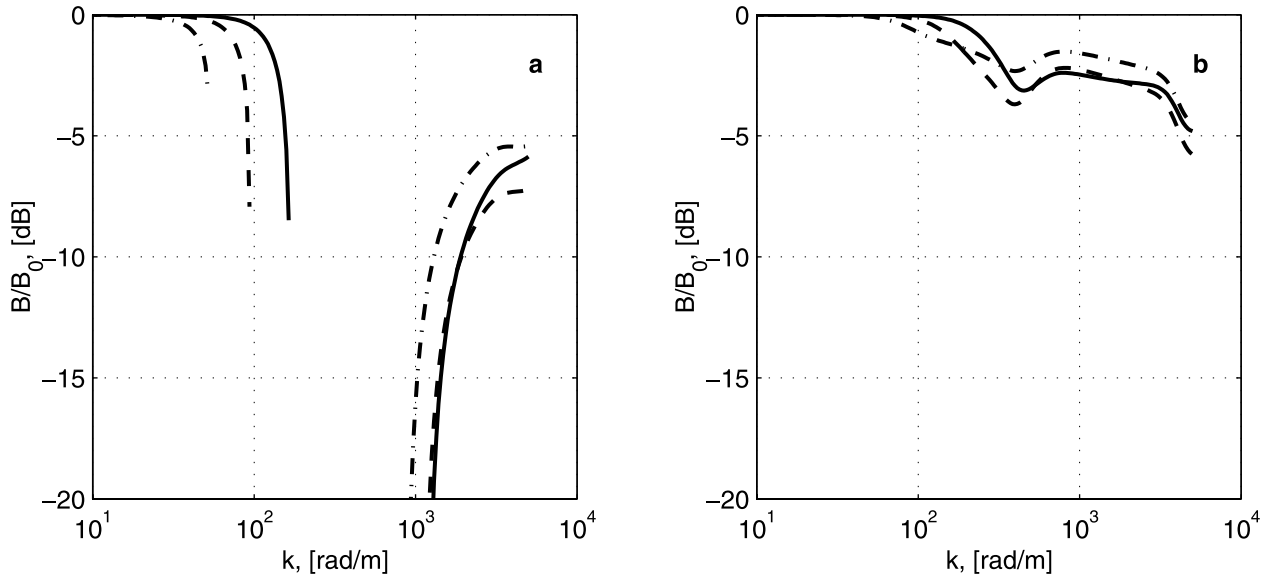
Figure 10. Contrasts in short wind waves spectrum caused by surface films of different elasticity 5 mN/m (solid lines), 10 mN/m (dashed lines), and 20 mN/m (dash-dotted lines) at wind (left) speed 5 m/s and (right) 15 m/s.

[*Gasparovich et al.*, 1988] experiments, and radar signatures of a surface current front [*Johannessen et al.*, 1997].

5.1. Internal Waves: JOWIP and SARSEX Experiments

[62] Overviews of the JOWIP and the SARSEX experiments are given by *Hughes and Dawson* [1988] and *Gasparovich et al.* [1988], respectively. Table 1 summarizes the observed parameters of IW (amplitude of IW orbital velocity, IW phase speed, and IW width), near-surface wind field conditions, and the geometry of the radar observations used in the model calculations.

5.1.1. JOWIP: TRW Run 81B

[63] During the JOWIP experiment, shipboard real aperture coherent radar studies of internal waves were carried out [*Kwoh et al.*, 1988]. Measurements at Run 81B were related to the packet of IW (consisting of about eight waves) traveling in the wind direction. At such conditions, surface manifestation of the IW should be well pronounced due to the resonance between the surface and internal waves (in that spectral interval where wave group velocity coincides with IW phase velocity). The measured X-band backscatter power and IW surface current velocity reproduced from *Kwoh et al.* [1988, Figure 10] are shown in Figure 11. These data demonstrate very strong modulation in short wind waves induced by IW. Observed peak over background (POB) ratio for the X-band radar scattering is varied from 10 to 50 (or from 10dB to 17dB).

[64] The model calculations performed for the measured IW surface current and conditions of the experiment listed in Table 1 (case 1) are also shown in Figure 11. The model consistently reproduces POB ratio; however, some phase shifts between the model and the measurements are apparent. According to the measurements, enhanced radar returns are located in the vicinity of the surface currents that oppose the wind direction, while in the model their locations are rather shifted toward the current convergence. In the surface areas where IW orbital velocity is positive (following the

Table 1. Parameters Used in the Model Calculations[a]

Case	IW C, u_m, L	Wind U, θ_w	Radar Band, Pol., θ, φ_R	Comments
1: JOWIP Run 81B (Ship observations)	$C = 0.5$ m/s, $u_m = 0.2$ m/s, $L = 60$ m	$U = 2.8$ m/s, $\theta_w = 0°$ (to)	X-band, HH pol., $\theta = 40°$, $\varphi_R = 173°$	IW packet, eight waves
2: JOWIP Run 71A (ship observation), also Run 12-3	$C = 0.7$ m/s, $u_m = 0.7$ m/s, $L^{-1} = 4 \cdot 10^{-2}$ m^{-1}	$U = 3.0$ m/s, $\theta_w = 118°$ (to)	X-, L-band, HH pol., $\theta = 32° - 37°$, $\varphi_R = -6°$	two IW solitons
3: SARSEX Wave packet G Waves G-2, G-3, G-4	$C = 0.7$ m/s, $u_{m2} = 0.52$ m/s $u_{m3} = 0.50$ m/s $u_{m4} = 0.33$ m/s $L_2^{-1} = 1.7 \cdot 10^{-2}$ m^{-1} $L_3^{-1} = 1.5 \cdot 10^{-2}$ m^{-1} $L_4^{-1} = 1.2 \cdot 10^{-2}$ m^{-1}	$U = 6.0$ m/s, $\theta_w = -145°$	X-, L-band, HH pol., $\theta = 35° - 45°$, $\varphi_R = -10°$	IW packet G: three solitons

[a]Note that in the table the wind and radar look directions are relative to the IW propagation direction. In the case of the solitons, L is the width of the model current defined by (60). In case 1, L and u_m are mean IW wavelength and amplitude of surface velocity induced by IW packet shown in Figure 11.
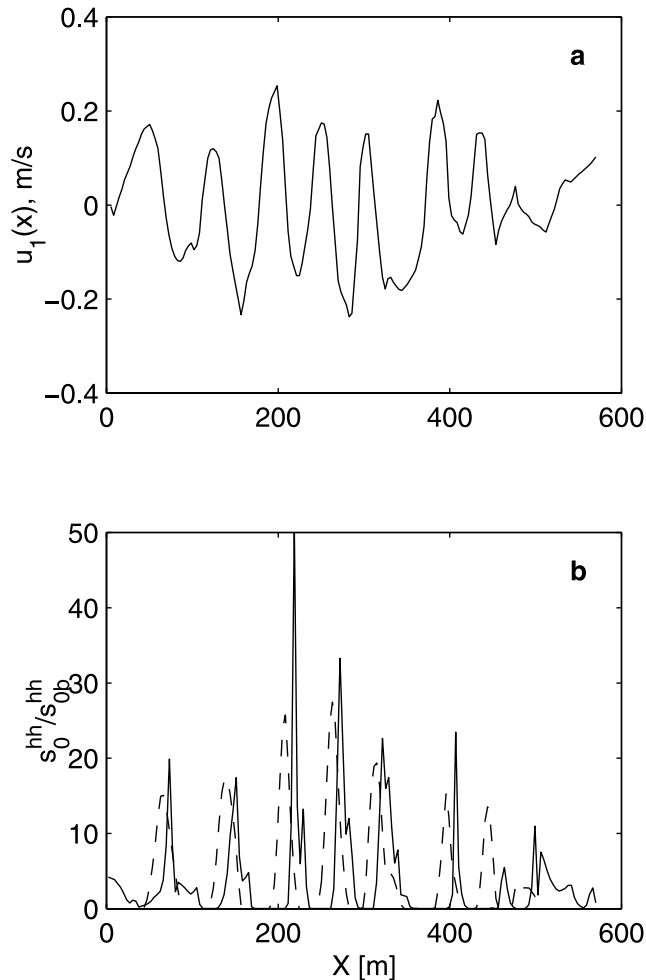
which provides weaker (in comparison with X-band) modulations in Bragg waves. The modulation of the L- and X-band NRCS at HH polarization and its components (Bragg, specular reflections from the "regular" surface and from breaking waves) normalized on the background level are plotted in Figures 12c and 12g. The peaks of the X-band NRCS modulations exceed the background level by up to 30 times (or 15 dB) and are shifted toward the current convergence. According to the model, 70% of the enhanced radar return is supported by Bragg scattering, and 30% is provided by specular reflection from enhanced wave breaking. Although the specular scattering from the "regular" surface is also increased in the convergence zone (as a consequence of the mean square slope (MSS) modulations), it does not play a dominant role in the generation of the peaks of the radar returns. Since strong modulation of Bragg waves results from the action of the wave breaking mechanism, we may conclude that the manifestation of IW in the X-band radar signal is caused by wave breaking modulations. In L-band, on the other hand, the role of breaking waves is not important. In L-band the modulation of the NRCS is governed by Bragg waves modulation, which results from the action of wave straining mechanism.

5.1.2. JOWIP: Run 12-3 (71A)

[66] During this run, two solitons of IW were observed. Unlike the previous case, the IW were traveling against the wind direction. The shipborne X-band radar signature of the soliton is shown in Figure 13. In this figure the radar data are taken from *Kwoh et al.* [1988, Figure 8], while the surface current is defined as

$$u(x, t) = u_m \sec h^2[(x - Ct)/L], \quad (60)$$

where the soliton width L, phase speed C, and maximum velocity u_m correspond to the measurements (leading soliton shown in Figure 8 of *Kwoh et al.* [1988]). The POB ratio in this case is also very high, attaining approximately 50 (or 15 dB). As was shown by *Kwoh et al.* [1988], the polarization ratio in the calm region was −6 dB, suggesting that the Bragg scattering predominates the radar signature. On the other hand, in the region of enhanced surface roughness (with visually observed wave breaking), the polarization ratio attains a value close to 1, confirming that the increase of radar returns is due to enhanced wave breaking and MSS. The ship mounted video recording support this conclusion.

[67] The model simulation of this run was done for the parameters of IW, wind conditions, and geometry of radar observations listed in Table 1 (case 2). The comparison of model IW radar signature and measurements is shown in Figure 13. Just as in the experiment, the model predicts very large amplitude of the backscatter power modulation. Though the model underestimates the measurements, in dB scale, observed and modeled POB ratio are quite close, 17 dB and 15 dB, correspondingly. Figure 14 illustrates the model peculiarities of the surface IW manifestation in more detail. Again, the wave breaking and MSS are significantly modulated by IW. In the region of maximum IW-induced surface current the amount of wave breaking is enhanced 6 times with respect to the background value. This results in an increased energy loss so that the wind wave energy just behind IW is decreased and wave breaking is totally suppressed. Strong wave breaking stimulates modulation of X-
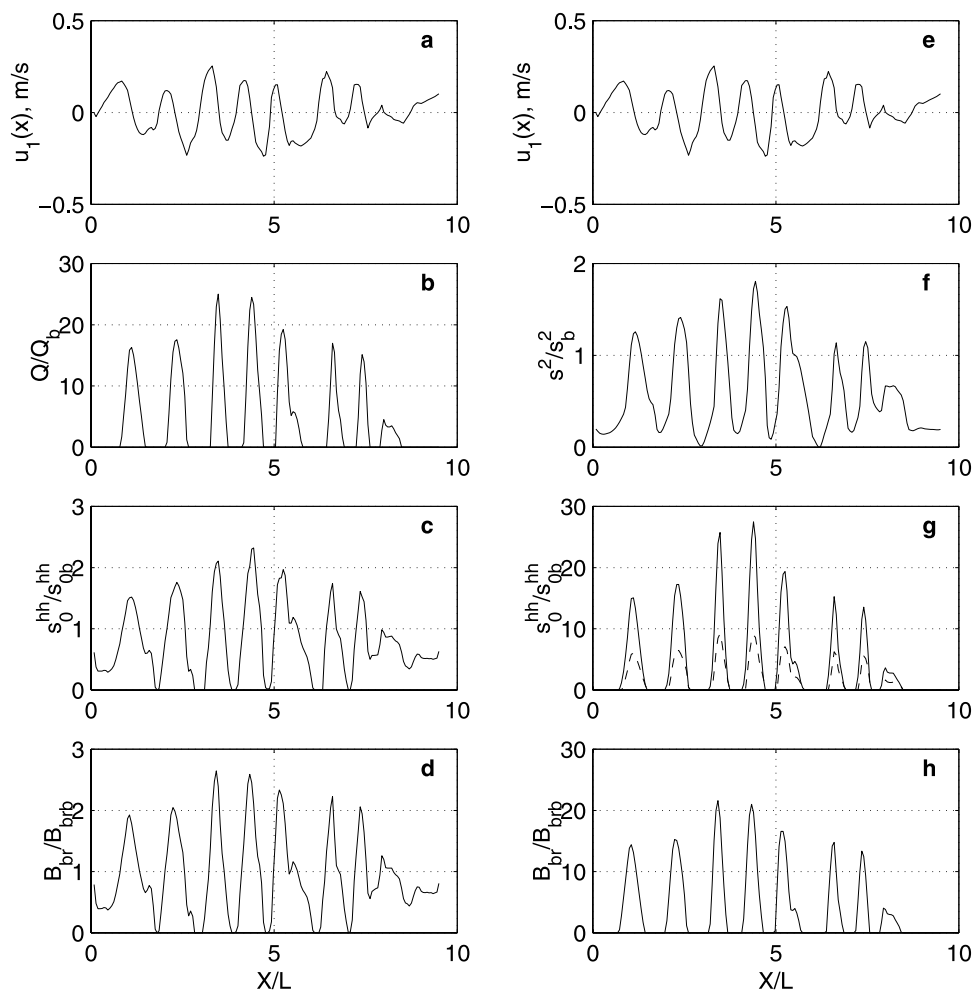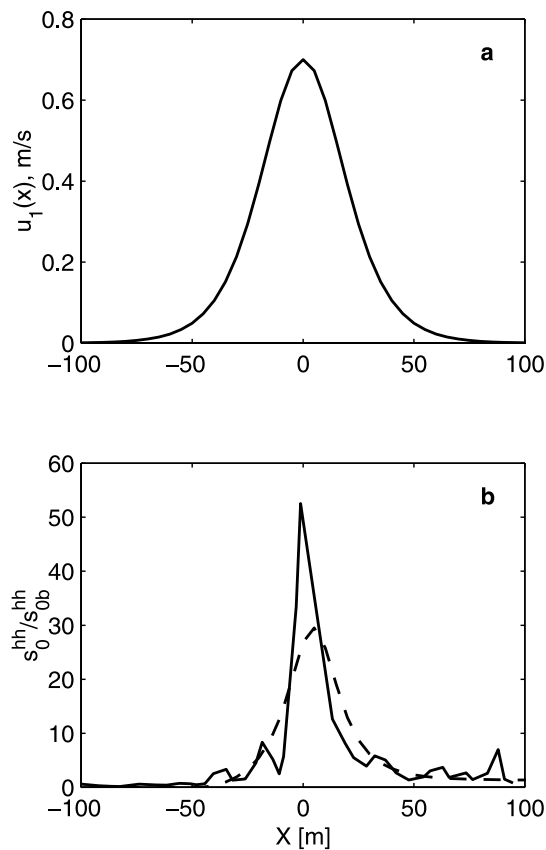
Figure 11. Measured and model HH, X-band radar signature of IW packet (case 1 in Table 1). (a) Measured surface velocity induced by IW. (b) Backscatter power normalized on the background value. Solid line is the measurements, dashed line is the model. The measurements are reproduced from *Kwoh et al.* [1988, Figure 10].

wind) the measured radar signal drops into the noise level, and the model radar scattering is almost vanished.

[65] Model calculations of the mean square slope, wave breaking, and Bragg waves modulations by the train of IW are shown in Figure 12. As can be seen, the mean square slope providing tilting of Bragg waves and supporting the quasi-specular reflections is significantly modulated by IW. However, the magnitude of wave breaking modulations is much stronger. Although wave breaking is fairly weak at low wind conditions, it becomes significantly enhanced (20 times) in the presence of the IW. According to the model, wave breaking contributes to the radar returns by means of both the specular reflections and the generation of Bragg scattering waves. In the X-band, strong modulation in wave breaking results in strong modulation of Bragg waves (see Figure 12h). Unlike at low winds, L-band Bragg waves are not sufficiently affected by wave breaking (recall that the interval of breaking waves affecting Bragg waves is $k < k_b/10$). Thus their modulations (see Figures 12h and 12d) are mainly governed by the wave straining mechanism

Figure 12. Model calculations of the sea surface manifestation of IW (case 1 in Table 1). (a) Measured surface velocity induced by IW. (b) Modulation of wave breaking. (c) Modulation of the HH, L-band NRCS. Contribution of specular reflection and wave breaking is small and not shown. (d) Modulation of L-band Bragg wave spectrum. (e) Same as in Figure 12a. (f) Modulation of the mean square slope. (g) Modulation of the HH, X-band NRCS: solid line is total NRCS, and dashed line is contribution of wave breaking. Contribution of specular reflection is small and not shown. (h) Modulation of X-band Bragg wave spectrum. All quantities are normalized on the corresponding background value.

Figure 13. The measured and the model HH, X-band radar signature of IW soliton (case 2 in Table 1). (a) Surface velocity induced by IW soliton. (b) Backscatter power normalized on the background value. Solid line is the measurements (reproduced from *Kwoh et al.* [1988, their Figure 8]); dashed line is the model.

band Bragg waves. Model simulations show that the direct effect of the IW on X-band Bragg waves (through straining effect) is small. Accounting for the wave breaking mechanism, on the other hand, results in a spectrum of Bragg waves 10 times more energetic in comparison with background level. In comparison, the modulation of L-band Bragg waves is mainly provided by their direct interaction with the current, whereas the effect of the wave breaking mechanism is small.

[68] IW significantly increases radar return both in X- and L-band. In X-band the peak-over-background ratio is 30 (or 15 dB), while in L-band it is around 10 (or 10 dB). At X-band, 60% of the increased radar returns results from Bragg scattering mechanism, and the rest is supported by both enhanced scattering from breaking waves and specular reflection due to enhanced mean square slope. In L-band, enhanced radar return is formed by Bragg scattering mechanism due to modulation of Bragg and tilting waves. Thus the scattering mechanisms responsible for the radar signature in X- and L-band are different, although they produce amplitude of radar modulation of the same order. This conclusion is consistent with the aircraft SAR observations discussed by *Shuchman et al.* [1988], where it was shown that these IW produce very similar signature for both X- and L-band with POB ratio of about 15 dB.

5.1.3. SARSEX: Wave Packet G

[69] During this experiment, trains of soliton-like IW were observed. The typical characteristics of three of these IW solitons (waves G-2, G-3, and G-4), the near-surface wind conditions, and the radar geometry used in model simulations are given in Table 1 (case 3). Unlike the JOWIP experiment, the radar signatures of IW in this experiment were observed at higher wind speed, while the wind direction in respect to the IW was approximately the same.

[70] Figure 15 presents section of X-band and L-band SAR images containing the radar signatures of waves G-2, G-3, and G-4, packet G. These data are reproduced from *Gasparovich et al.* [1988, Figure 12]. The surface current velocity induced by IW are model calculations of (60) with maximum surface current and IW solitons width as they are listed in *Gasparovich et al.*'s [1988] Table 1 (Bartlet Track). In total, the model radar signatures shown in Figure 15 are consistent with the measurements. The model correctly reproduces the POB ratio, which is almost the same in both X- and L-bands. However, an overestimate of model radar signature for the first soliton (wave G-2) is apparent. Contribution of the different mechanisms to the radar signature of wave G-3 (the middle soliton in Figure 15) is shown in Figure 16. As in the previous cases, both wave breaking and MSS are significantly modulated by the IW. Comparing Figures 16 and 14, one can mention that at higher wind speed the enhancement of wave breaking is shifted on the forward face of IW, i.e., toward the convergence of the current. Furthermore, the zone of wave breaking suppression becomes narrower. The modulation of X-band and L-band Bragg waves is still rather strong, and again the X-band Bragg wave modulations results from wave breaking mechanism, while in L-band the straining mechanism dominates wave modulations.

[71] The peak-over-background ratio for the X- and L-bands is 3 and 2, correspondingly (or approximately 5 and 3 dB). In X-band the peak of radar modulations results from equivalent contribution of Bragg scattering and scattering from breaking waves. In contrast, in L-band the peak modulation is provided by Bragg scattering mechanism only. Thus X-band and L-band signatures of the same IW have approximately the same shape and magnitude of the contrast. This was found in all studies devoted to the analysis of JOWIP and SARSEX experiments.

5.2. Sea Front: CoastWatch-95 Experiment

[72] During the ''CoastWatch-95'' experiment [*Johannessen et al.*, 1997], ERS-2 SAR images and in situ observations (meteorological parameters, surface current velocity, sea temperature and salinity in the upper layer) were collected nearly simultaneously over the Norwegian coastal current (NCC). Here we attempt to simulate the ERS-2 SAR image obtained at 10:31 on 27 September 1995 (orbit 2281, frame 2439). In this case the time gap between the SAR image and in situ measurements taken from the ship crossing the front was just 21 min. A fragment of the SAR image is shown in Figure 17. The accompanying in situ measurements along ship route (indicated on SAR image) are presented in Figure 18. As seen, the surface temperature T_w dropped about 4° across the front. In addition the surface current was jet-like along the frontal zone. However, significant changes of the cross front
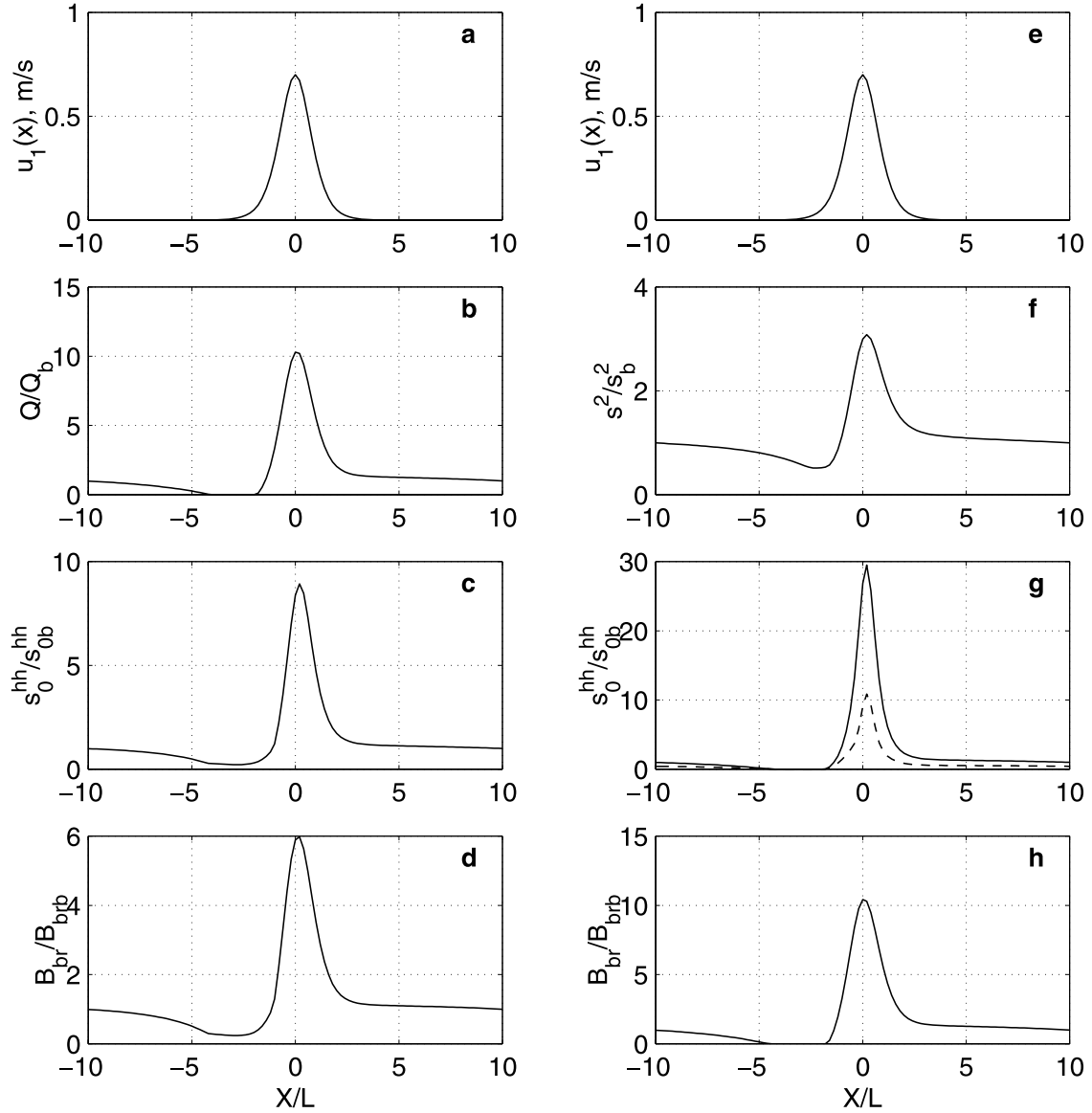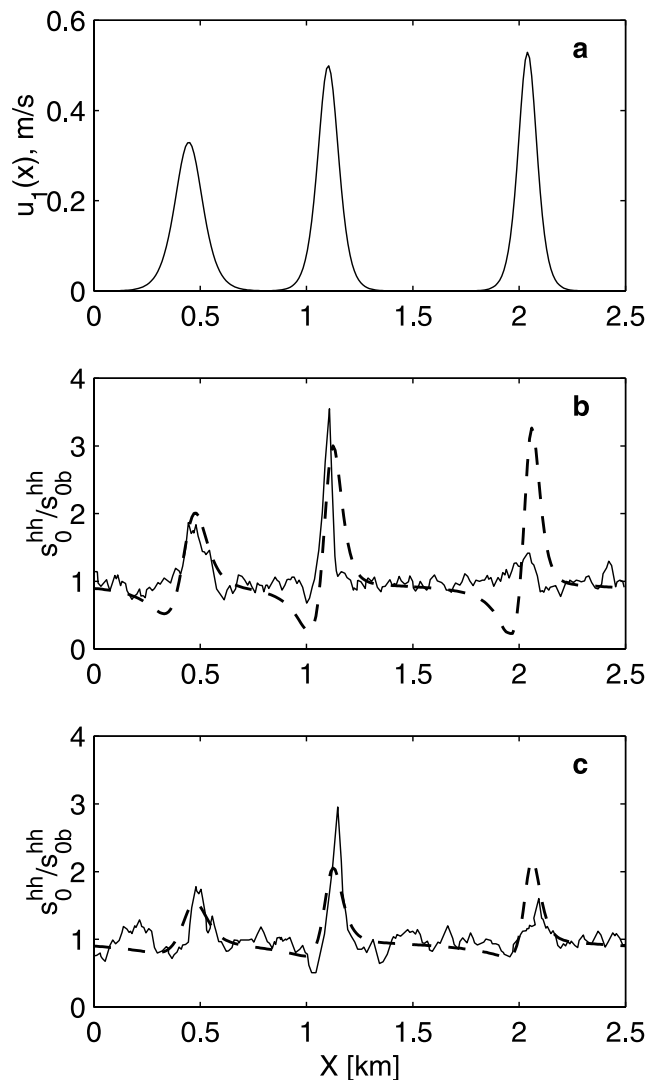
Figure 14. Model calculations of the sea surface manifestation of IW soliton (case 2 in Table 1). (a) Current velocity induced by IW on the sea surface. (b) Modulation of wave breaking. (c) Modulation of L-band NRCS at HH polarization. Solid line for total NRCS coincides with the line for Bragg scattering. Contribution of specular reflection and wave breaking is negligible. (d) Modulation of L-band Bragg wave spectrum. (e) Same as in Figure 14a. (f) Modulation of the mean square slope. (g) Modulation of X-band NRCS at HH polarization: solid line is total NRCS, and dashed line is sum of quasi-specular and wave breaking contributions. (h) Modulation of X-band Bragg wave spectrum. All quantities are normalized on the corresponding background value.

Figure 15. Measured and model HH, X- and L-band radar signature of train of IW solitons (case 3 in Table 1). (a) Surface velocity induced by IW solitons. (b) Section of the X-band SAR image normalized on the background level. Solid line is the measurements (reproduced from *Gasparovich et al.* [1988, Figure 12]), and dashed line is the model. (c) Same as in Figure 15b, but for the L-band SAR image.

surface temperature front. The measured near surface wind speed does not exhibit a behavior that could explain the observed radar signatures in the vicinity of the front.

[73] The measured surface temperature and current velocities shown in Figure 18 were used to simulate the NRCS of the sea surface. To obtain the near-surface wind stress as the input parameter for the wind waves, we have modeled the transformation of the MABL across the front using a mean sea surface temperature $T_w = 13.5°C$, air temperature of $T_a = 12.5°C$ and a mean wind speed $U_h = 9.5$ m/s at the upwind (warm) side of the front. Since the stratification of the atmospheric boundary layer on the warm side of the front was unstable (a well-mixed MABL), the measured air temperature was related to the potential temperature of the upper bound of the MABL, i.e., $T_D = T_a$. Then the resistance law (55) was used to estimate the geostrophic wind velocity G as the input parameter for the calculations of MABL transformation. It is moreover assumed that G and T_D are constant over the sea front. The friction velocity in each point across the front for the constant values of G and T_D, but for the varying surface temperature T_w are then calculated. The results are shown in Figure 19. The adjustment of the atmospheric boundary layer to the "cold" sea surface temperature on the downwind side of the front results in a decrease of the wind speed and air temperature. These effects were also observed, though in the model calculations they are more pronounced. A possible reason is that the measurements from the ship crossing the front was undertaken during 2 hours, and during this time, atmospheric variability could have smeared out the effect of the ABL transformation.

[74] The simulated mean square slope, wave breaking, and spectrum of Bragg waves across the front are plotted in Figure 20. The dashed lines show the "pure" effect of changes of the MABL stratification, while the solid lines show the "pure" effect of the current (when the wind field is uniform). The decrease of the wind stress on the cold side of the front causes a decrease of the mean square slope, wave breaking, and Bragg waves. The surface current gives an additional contribution to wave transformation. The effect of the current on the wave breaking is stronger than on the mean square slope. Moreover, the modulation of wave breaking causes modulation of Bragg waves. It is also apparent that when the wave breaking mechanism is switched off, the effect of the current of the Bragg waves is negligible (due to small relaxation time). Comparing Figure 20b with Figures 20a, 20c, and 20d, we can conclude that the enhanced wave breaking and generation of Bragg waves (via modulation of wave breaking) as well as the increase in mean square slope are occurring in the area of the surface current convergence. On the other hand, the effect of the current shear appears not to be significant.

[75] The simulated and observed radar signatures of the front are shown in Figure 21. The model calculations were done for C-band, VV polarization, $\theta = 23°$. Radar look direction is indicated in Figure 17. The dashed line in Figure 21b demonstrates the effect of the MABL stratification only, which results in stronger radar scattering on the warm side of the front due to enhanced boundary layer turbulence and friction velocity. The solid line shows the joint atmospheric and current effect on the radar scattering. Figure 21c demonstrates the simulated impact of different
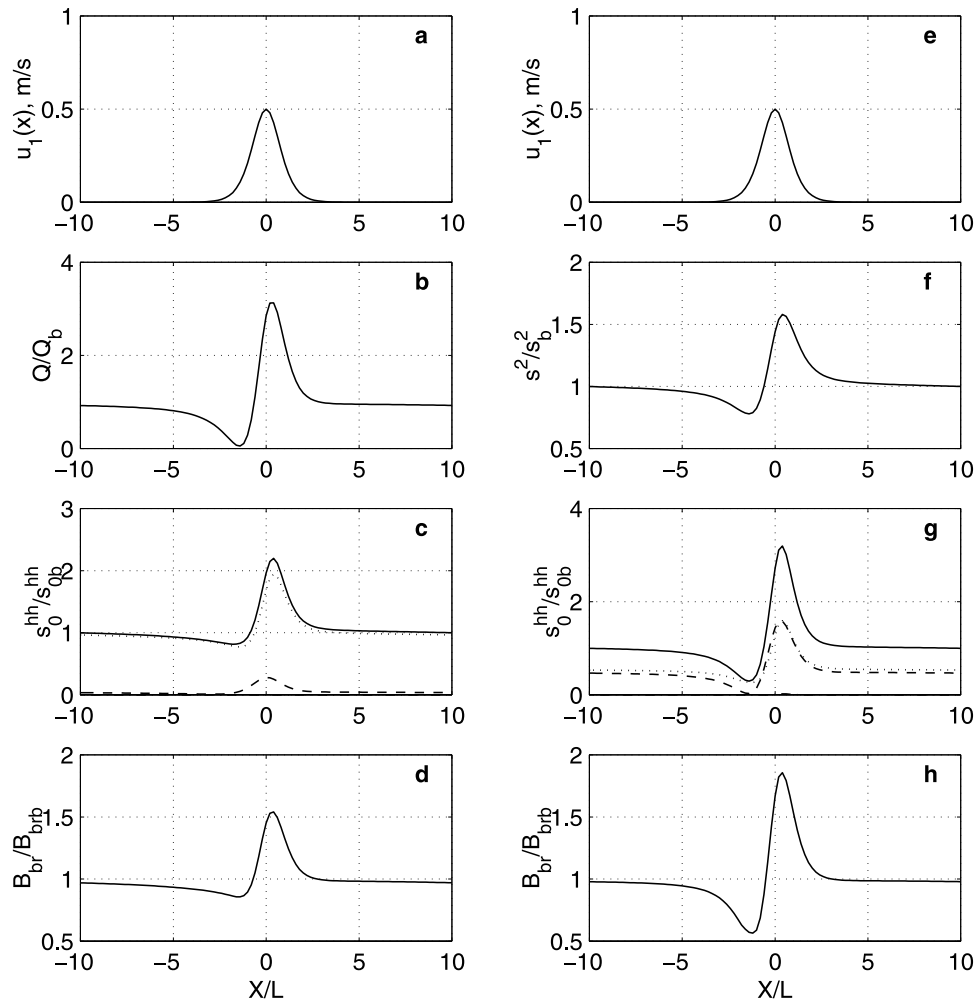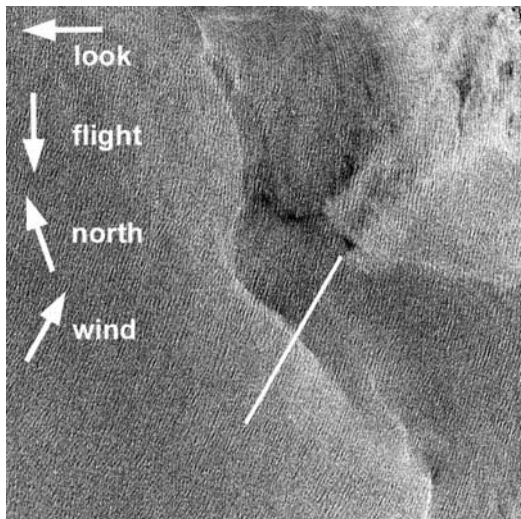
current component were also observed. In particular, in the vicinity of the temperature front the sea surface current is directed perpendicular to the front (from cold to warm water), leading to a surface current convergence. The atmospheric boundary layer stratification was unstable in the warm sector and stable in the cold sector. At the same time the wind direction was steady at a speed around 9.5 m/s. However, referring to Figure 18b, one may see that in the cold sector the mean near surface wind speed decreased, presumably due to the effect of the atmospheric stratification. The section of the SAR image along the ship track (shown in Figure 17) is presented in Figure 18d reveals higher radar scattering at the warm side of the front, and the locally enhanced radar returns in the vicinity of the sea

Figure 16. Model calculations of the sea surface manifestation of the IW soliton (case 3 in Table 1, wave G-3). (a) Current velocity induced by IW on the sea surface. (b) Modulation of wave breaking. (c) Modulation L-band NRCS at HH polarization: solid line is total NRCS, and dashed line is wave breaking contribution. Contribution of specular reflection is negligible and not shown. (d) Modulation of L-band Bragg wave spectrum. (e) Same as Figure 16a. (f) Modulation of the mean square slope. (g) Same as in Figure 16c, but for the X-band. (h) Modulation of X-band Bragg wave spectrum. All quantities are normalized on the corresponding background value.

scattering mechanisms on the radar return. As follows from this plot, the Bragg scattering is the dominating mechanism, providing about 80% of radar return power on the upwind side of the front. In the vicinity of the front the mean square slope and wave breaking are enhanced, and relative contributions of specular reflection from the "regular" surface and wave breaking to the NRCS are thus increased. Moreover, the enhanced wave breaking generates enhanced spectrum of Bragg waves, which in turn further increases the radar signature. Since the sea surface roughness is enhanced in the convergence zone and suppressed in the divergence zone, the modulation of the radar returns mainly follows the current divergence field. Overall, the simulated radar signature of the sea front is consistent with the SAR observation.

6. Conclusion

[76]　In the present paper we propose a new radar imaging model of oceanic features of arbitrary origin. This model is the extension of semi-empirical model of the normalized radar cross section (NRCS) of the sea surface developed by *Kudryavtsev et al.* [2003a] in the case of the nonuniform medium. It takes into account scattering from "regular"
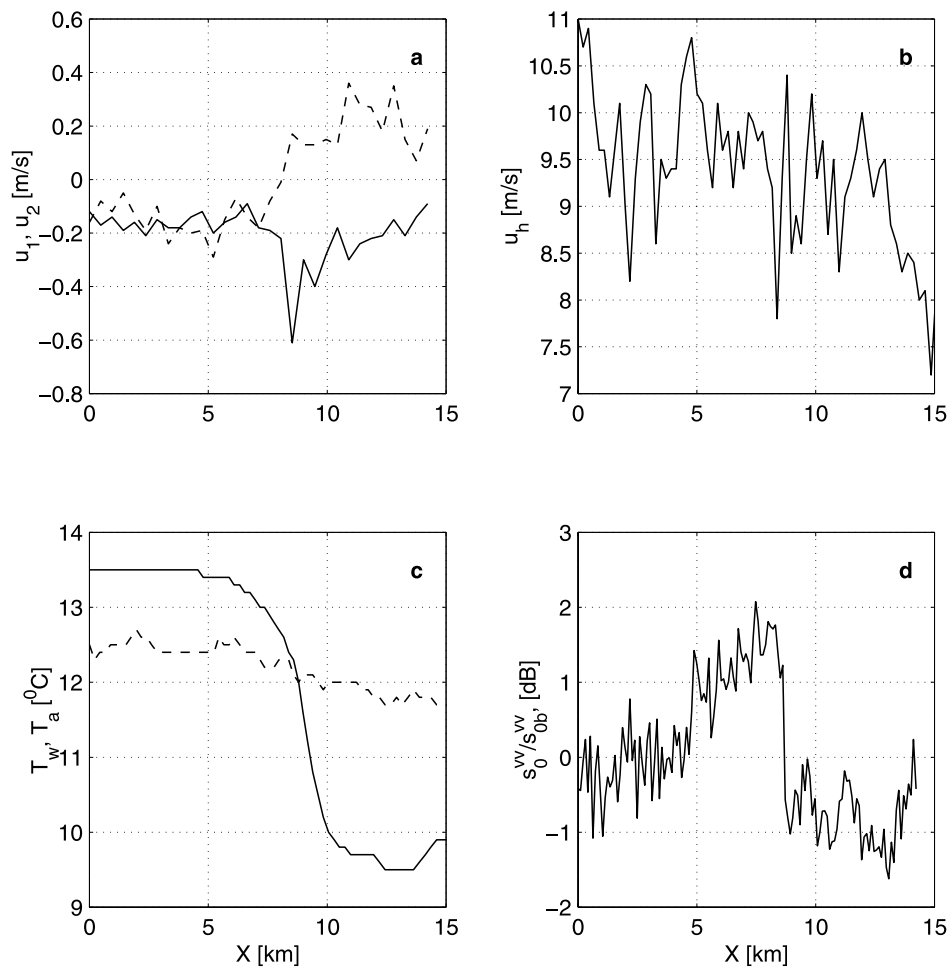

Figure 17. A fragment of ERS-2 SAR image of Norwegian coastal current obtained at 1031 UT on 27 September 1995. Arrows indicate wind, radar look, and north direction. White line is the ship route where measurements shown in Figure 18 were done.

Figure 18. Measurements taken from the ship crossing the sea front along the line shown in SAR image, Figure 17. (a) Components of the current velocity parallel (dashed line) and perpendicular (solid line) to the front. (b) Wind speed at height of 15 m. (c) Sea surface temperature (solid line) and air temperature (dashed line) at height of 15 m. (d) Section of SAR images (normalized on the mean value) taken along ship route.
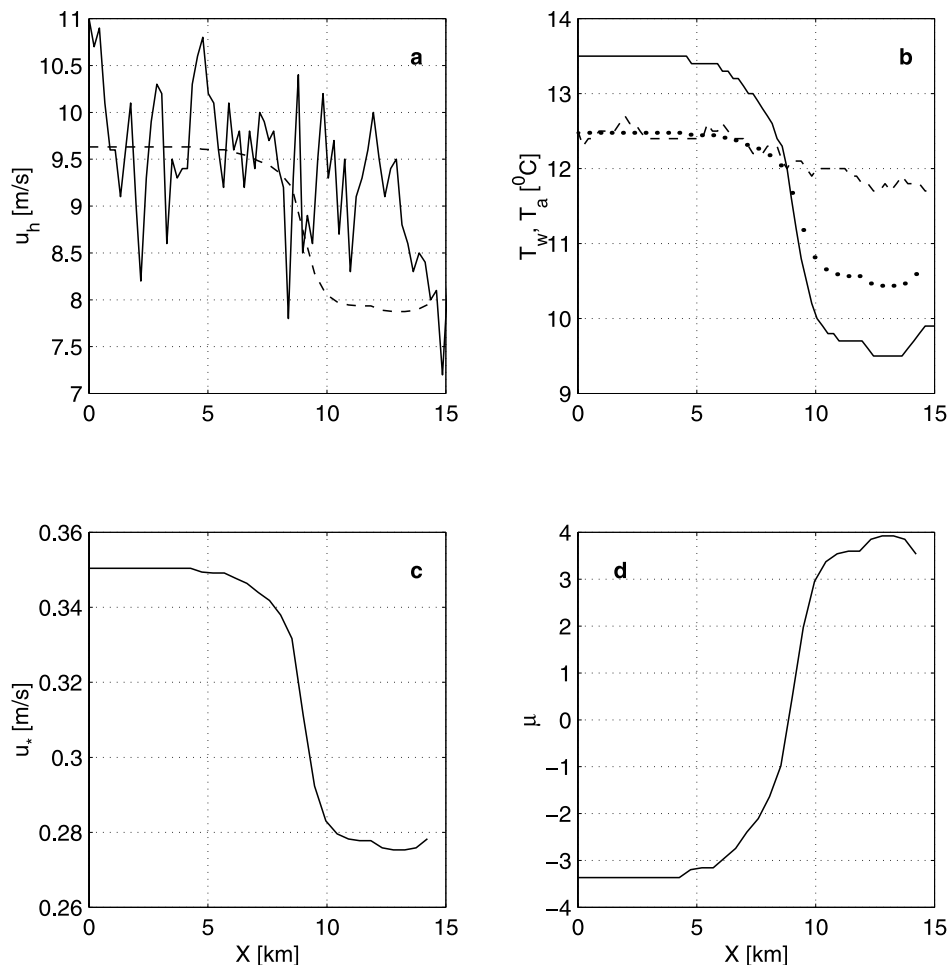
Figure 19. Modeled and measured atmospheric parameters over the sea front. (a) Modeled (dashed line) and observed (solid line) wind speed. (b) Modeled (dotted line) and observed (dashed line) air temperature. Solid line is sea surface temperature. (c) Modeled air friction velocity. (d) Parameter of MABL stratification (equation (56)).

surface (by means of resonant Bragg scattering and specular reflections) and specular reflection from breaking waves. Description of wind waves is based on solution of the energy balance equation, where wind forcing, energy dissipation due to viscosity and wave breaking, and nonlinear wave interactions are taken into account. The latter, in particular, includes the mechanism of short wave generation by breaking crests of longer surface waves, proposed by *Kudryavtsev and Johannessen* [2004].

[77] Breaking waves play a key role in the radar imaging model. They (1) scatter radio waves (thus directly contributing to the NRCS), (2) provide energy dissipation of wind waves (thus defining the wave spectrum of intermediate scale waves), and (3) additionally generate short surface waves (thus affecting Bragg scattering). In the model, the wave breaking characteristics are expressed in terms of the same wave breaking statistics introduced by *Phillips* [1985]. It gives a consistency between radar scattering and the sea surface components of the radar imaging model.

[78] Transformation of wave spectrum in nonuniform medium is found as a solution of the wave action conservation equation written in the relaxation approximation. Unlike other studies, relaxation time is not specified arbi-

trary, but directly related to the wave energy source producing background wave spectrum. Such definition gives consistency between the background spectrum and wave breaking and their evolution in nonuniform medium. It is shown that modulation of wave breaking significantly influences modulation of shorter wind waves. In the range of short waves related to Ku-, X-, and C-bands the mechanism of Bragg waves modulation through wave breaking is the governing mechanism. Effect of direct interaction of Bragg waves with the current (straining mechanism) is negligible, while the mechanism of short wave modulations via wave breaking gives significant spectral contrast.

[79] Surface current, varying near surface wind field, and surfactants are considered as the main sources of the medium nonuniformity. In such cases when an oceanic features is accompanied with varying surface temperature (e.g., oceanic front), varying wind field results from the transformation of the planetary atmospheric boundary layer over sea surface temperature. The effect of the atmospheric boundary layer is taken into accounted through the resistance law for the planetary boundary layer. Impact of surfactants (which can be accumulated in the zones of surface current convergence) on short wind waves is in-
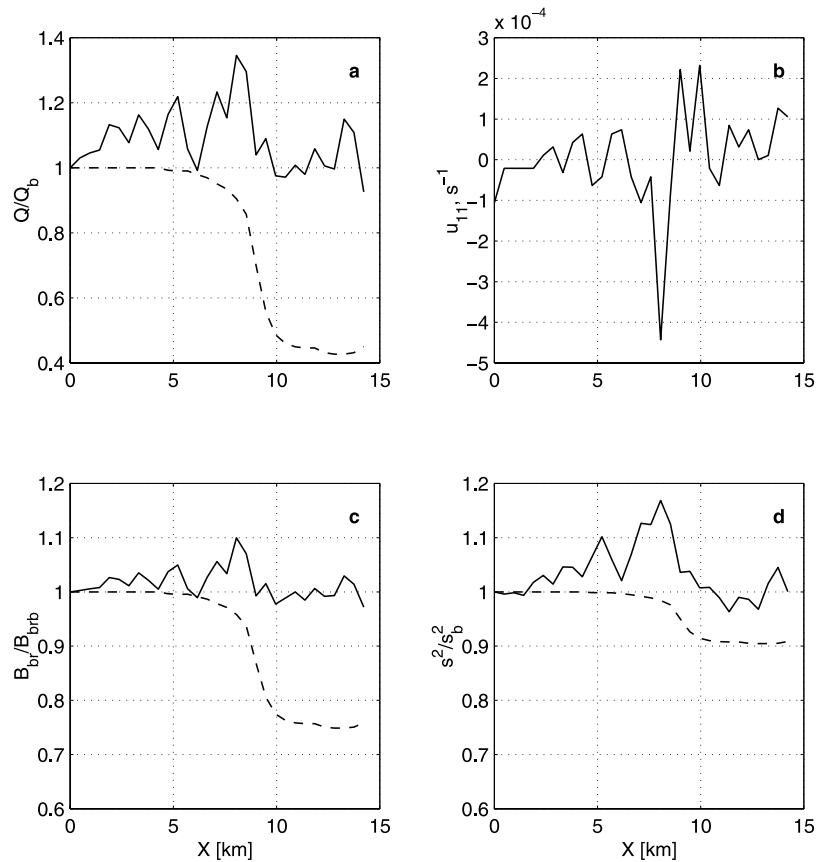
Figure 20. Profiles of (a) wave breaking, (b) surface current divergence, (c) C-band Bragg wave spectrum, and (d) mean square slope over the sea front. Solid lines in Figures 20a, 20c, and 20d) show variations of the sea surface parameters caused by the effect of the surface current only, while the dashed lines show effect of the MABL stratification only.

cluded in the model through the effective viscosity coefficient depending of surface film elasticity.

[80] The model is tested against well-controlled experiments JOWIP and SARSEX on internal waves and the experiment "CoastWatch-95" on radar signatures of surface features within the Norwegian coastal current. A reasonably

good agreement between model and observations was obtained. In particular, the model is able to explain the observed similarity between radar signatures of internal waves in L- and X-bands. Model calculations show that in L-band the modulation of Bragg waves is responsible for the radar signature, while in X-band the effect of wave
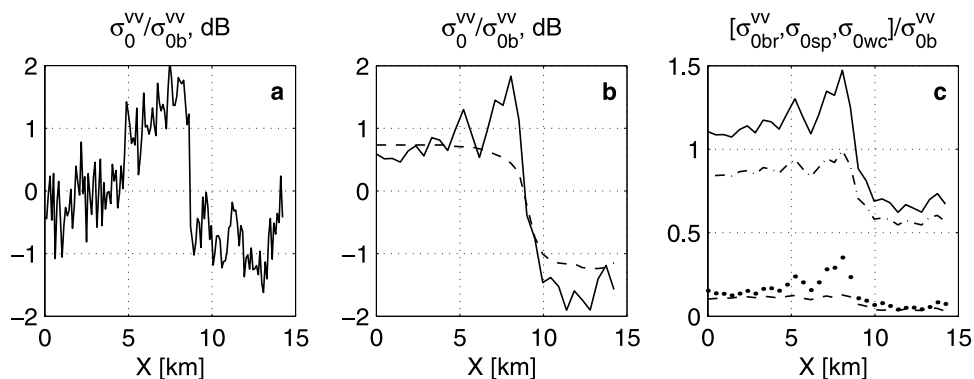

Figure 21. (a) Section of the ERS-2 SAR image (normalized on mean value) along the line shown in Figure 17. (b) Modeled NRCS over the front (normalized on mean value). (c) Relative contribution of different scattering mechanism (normalized on mean NRCS): solid line is total NRCS, dash-dotted line is contribution of Bragg scattering, dashed line is contribution of wave breaking, and dotted line is contribution of specular reflection.

breaking through additional generation of Bragg waves and non-Bragg radar scattering dominates radar signatures. Moreover, model simulation of the ''CoastWatch-95'' experiment showed that the governing mechanisms responsible for the radar signature of the ocean front are transformation of planetary atmospheric boundary layer over the surface temperature front and wave breaking which is enhanced in the zones of the surface current convergent.

References

Alpers, W., and I. Hennings (1984), A theory of the imaging mechanism of underwater bottom topography by real and synthetic aperture radar, *J. Geophys. Res.*, *89*(C6), 10,529–10,546.

Bahar, E. (1981), Scattering cross section for composite random surface: Full wave analysis, *Radio Sci.*, *16*(6), 1327–1335.

Beal, R. C., I. Katz, and P. DeLeonibus (Eds.) (1981), *Spaceborne SAR for Oceanography*, Johns Hopkins Univ. Press, Baltimore, Md.

Beal, R., V. Kudryavtsev, D. Thompson, S. Grodsky, D. Tilley, V. Dulov, and H. Graber (1997), The influence of the marine atmospheric boundary layer on ERS-1 synthetic aperture radar imagery of the Gulf Stream, *J. Geophys. Res.*, *102*(C3), 5799–5814.

Bentamy, A., Y. Quilfen, P. Queffeulou, and A. Cavanie (1994), Calibration and validation of ERS-1 scatterometer, *Tech. Rep. DRO-OS-94-01*, Inst. Fr. Rech. pour l'Exploit. de la Mer (IFREMER), Brest, France.

Brown, R. (1982), On two-layer models and the similarity functions for the PBL, *Boundary Layer Meteorol.*, *24*, 451–463.

Chubb, S., A. Cooper, R. Jansen, R. Fusina, and J. Lee (1999), Radar backscatter from breaking waves in Gulf Stream current convergence fronts, *IEEE Trans. Geosci. Remote Sens.*, *17*(4), 1951–1965.

Cooper, A. L., S. R. Chubb, F. Askari, G. R. Valenzuela, J. R. Bennett, and W. C. Keller (1994), Radar surface signatures for the two-dimensional tidal circulation over Phelps Bank, Nantucket shoals: A comparison between theory and experiment, *J. Geophys. Res.*, *99*(C4), 7865–7883.

da Silva, J. C., S. A. Ermakov, I. S. Robinson, D. R. Jeans, and S. V. Kijashko (1998), Role of surface films in ERS SAR signatures of internal waves on the shelf: 1. Short-period internal waves, *J. Geophys. Res.*, *103*(C4), 8009–8032.

Donelan, M., and W. Pierson (1987), Radar scattering and equilibrium ranges in wind-generated waves with application to scatterometry, *J. Geophys. Res.*, *92*(C5), 4971–5029.

Donelan, M. A., J. Hamilton, and W. H. Hui (1985), Directional spectra of wave generated waves, *Philos. Trans. R. Soc. London, Ser. A, 315*, 509–562.

Elfouhaily, T., B. Chapron, K. Katsaros, and D. Vandermark (1997), A unified directional spectrum for long and short wind driven waves, *J. Geophys. Res.*, *102*(C7), 15,781–15,796.

Ermakov, S. A., S. G. Salashin, and A. R. Panchenko (1992), Film slicks on the sea surface and some mechanisms of their formation, *Dyn. Atmos. Oceans*, *16*, 279–304.

Espedal, H. A., O. M. Johannessen, J. A. Johannessen, E. Dano, D. R. Lyzenga, and J. C. Knulst (1998), COASTWATCH'95: ERS 1,2 SAR detection of natural film on the ocean surface, *J. Geophys. Res.*, *103*(C11), 24,969–24,982.

Gasparovich, R. F., J. A. Apel, and E. S. Kasischke (1988), An overview of the SAR internal wave signature experiment, *J. Geophys. Res.*, *93*(C10), 12,304–12,316.

Holliday, D., G. St-Cyr, and N. W. Woods (1986), A radar ocean imaging model for small to moderate incidence angles, *Int. J. Remote Sens.*, *7*, 1809–1834.

Hughes, B. A. (1978), The effect of internal waves on surface wind waves: 2. Theoretical analysis, *J. Geophys. Res.*, *83*(C1), 455–465.

Hughes, B. A., and T. W. Dawson (1988), Joint Canada–U. S. wave investigation project: An overview of the Georgia Strait experiment, *J. Geophys. Res.*, *93*(C10), 12,219–12,234.

Jansen, R., C. Shen, S. Chubb, A. Cooper, and T. Evans (1998), Subsurface, surface, and radar modeling of a Gulf Stream current convergence, *J. Geophys. Res.*, *103*(C9), 18,723–18,743.

Johannessen, J., R. Shuchman, G. Digranes, D. Lyzenga, W. Wackerman, O. Johannessen, and P. Vachon (1996), Coastal ocean fronts and eddies imaged with ERS-1 synthetic aperture radar, *J. Geophys. Res.*, *101*(C3), 6651–6667.

Johannessen, O. M., E. Korsbakken, P. Samuel, A. D. Jenkins, and H. Espedal (1997), COAST WATCH: Using SAR imagery in an operational system for monitoring coastal currents, wind, surfactants and oil spills, in *Operational Oceanography: The Challenge for European Co-operation, Oceanogr. Ser.*, vol. 62, edited by J. H. Stel, Elsevier, New York.

Komen, G. J., L. Cavalery, M. Donelan, K. Hasselmann, and P. A. E. M. Janssen (1994), Dynamics and modelling of ocean waves, 540 pp., Cambridge Univ. Press, New York.

Kudryavtsev, V. (1994), The coupling of wind and internal waves: Modulation and friction mechanism, *J. Fluid Mech.*, *278*, 33–62.

Kudryavtsev, V., and J. Johannessen (2004), On effect of wavebreaking on short wind waves, *Geophys. Res. Lett.*, *31*, L20310, doi:10.1029/2004GL020619.

Kudryavtsev, V. N., S. A. Grodsky, V. A. Dulov, and A. N. Bol'shakov (1995), Observations of wind waves in the Gulf Stream frontal zone, *J. Geophys. Res.*, *100*(C10), 5826–5839.

Kudryavtsev, V., S. Grodsky, V. Dulov, and V. Malinovsky (1996), Observation of atmospheric boundary layer evolution above the Gulf Stream frontal zone, *Boundary Layer Meteorol.*, *79*, 51–82.

Kudryavtsev, V., V. Malinovsky, and A. Rodin (1999), Manifestations of sea surface temperature fronts on radar imagery (in Russian), *Earth Observ. Space*, *6*, 16–26.

Kudryavtsev, V., D. Hauser, G. Caudal, and B. Chapron (2003a), A semi-empirical model of the normalized radar cross-section of the sea surface: 1. The background model, *J. Geophys. Res.*, *108*(C3), 8054, doi:10.1029/2001JC001003.

Kudryavtsev, V., D. Hauser, G. Caudal, and B. Chapron (2003b), A semi-empirical model of the normalized radar cross-section of the sea surface: 2. Radar modulation transfer function, *J. Geophys. Res.*, *108*(C3), 8055, doi:10.1029/2001JC001004.

Kwoh, D. S. W., B. M. Lake, and H. Rungaldier (1988), Microwave scattering from internal wave modulated surface waves: A shipboard real aperture coherent radar study in the Georgia Strait experiment, *J. Geophys. Res.*, *93*(C10), 12,235–12,248.

Levich, V. G. (1962), *Physiochemical Hydrodynamics*, Prentice-Hall, Upper Saddle River, N. J.

Lyzenga, D. R. (1996), Effects of wave breaking on SAR signatures observed near the edge of the Gulf Stream, in *Proceedings of International Geoscience and Remote Sensing Symposium*, pp. 908–910, IEEE Press, Piscataway, N. J.

Lyzenga, D. R., and J. R. Bennett (1988), Full-spectrum modeling of synthetic aperture radar internal wave signature, *J. Geophys. Res.*, *93*(C10), 12,345–12,354.

Marmorino, G. O., R. W. Jansen, G. R. Valenzuela, C. L. Trump, J. S. Lee, and J. A. C. Kaiser (1994), Gulf Stream surface convergence imaged by synthetic aperture radar, *J. Geophys. Res.*, *99*(C9), 18,315–18,328.

Phillips, O. M. (1977), *The Dynamics of the Upper Ocean*, Cambridge Univ. Press, New York.

Phillips, O. M. (1985), Spectral and statistical properties of the equilibrium range in wind-generated gravity waves, *J. Fluid Mech.*, *156*, 505–531.

Plant, W. J. (1990), Bragg scattering of electromagnetic waves from the air/sea interface, in *Surface Waves and Fluxes*, vol. II, *Remote Sensing*, edited by G. L. Geernaert and W. J. Plant, pp. 41–108, Springer, New York.

Romeiser, R., and W. Alpers (1997), An improved composite surface model for the radar backscattering cross section of the ocean surface: 2. Model response to surface roughness variations and the radar imaging of underwater bottom topography, *J. Geophys. Res.*, *102*(C11), 25,251–25,267.

Shuchman, R. A., D. R. Lyzenga, B. M. Lake, B. A. Hughes, R. F. Gasparovich, and E. S. Kasischke (1988), Comparison of joint Canada–U. S. ocean wave investigation project synthetic aperture radar data with internal wave observations and modeling results, *J. Geophys. Res.*, *93*(C10), 12,283–12,291.

Snyder, R. L., and R. M. Kennedy (1983), On the formation of whitecaps by a threshold mechanism: 1. Basic formation, *J. Phys. Oceanogr.*, *13*, 1482–1492.

Stewart, R. W. (1974), The air-sea momentum exchange, *Boundary Layer Meteorol.*, *6*, 151–167.

Thompson, D. R. (1988), Calculation of radar backscatter modulations from internal waves, *J. Geophys. Res.*, *93*(C10), 12,371–12,380.

Thompson, D. R., B. L. Cotwols, and R. E. Sterner (1988), A comparison of measured surface wave spectral modulations with predictions from a wave-current interaction model, *J. Geophys. Res.*, *93*(C10), 12,339–12,343.

Vachon, P. W., and F. W. Dobson (2000), Wind retrieval from RADARSAT SAR images: Selection of a suitable C-Band HH polarization wind retrieval model, *Can. J. Remote Sens.*, *26*(4), 306–313.

Valenzuela, G. R., M. B. Laing, and J. C. Daley (1971), Ocean spectra for the high frequency waves as determined from airborne radar measurements, *J. Mar. Res.*, *29*(2), 69–84.

Venkatram, A. A. (1977), Models of internal boundary layer development: A review, *Boundary Layer Meteorol.*, *11*, 419–438.

Vogelzang, J., G. L. Wensink, M. W. van der Kooij, and G. van der Burg (1991), Sea bottom topography with polarimetric P-, L-, and C-band SAR, *Tech. Rep. BCRS Rep. 91-40*, 45 pp., Neth. Remote Sens. Board, Delf, Netherlands.

Voronovich, A. G., and V. U. Zavorotny (2001), Theoretical model for scattering of radar signals in ku- and c-bands from a rough sea surface with breaking waves, *Waves Random Media*, *11*, 247–269.

Walker, D. T., D. R. Lyzenga, E. Ericson, and D. E. Lung (1996), Radar backscatter and surface roughness measurements from stationary breaking waves, *Philos. Trans. R. Soc. London, Ser. A*, *452*, 1953–1984.

Wentz, F. J., and D. K. Smith (1999), A model function for the ocean-normalized radar cross-section at 14 GHz derived from NSCAT observations, *J. Geophys. Res.*, *104*(C5), 11,499–11,514.

Wetzel, L. B. (1986), On microwave scattering by breaking waves, in *Wave Dynamics and Radio Probing of the Ocean Surface*, edited by O. M. Phillips and K. Hasselmann, pp. 273–284, Springer, New York.

Zilitinkevich, S. S. (1970), *Dynamics of the Atmospheric Boundary Layer*, Gidrometeoizdat, St. Petersburg, Russia.

————————————

D. Akimov and V. Kudryavtsev, Nansen International Environmental and Remote Sensing Center, 26/28 Bolshaya Monetnaya Str., 19701 St. Petersburg, Russia. (dmitry.akimov@niersc.spb.ru; vladimir.kudryavtsev@niersc.spb.ru)

B. Chapron, Institute Francais de Recherche pour I'Exploitation de la Mer, Technopole Brest Iroise, BP 70, F-29280 Plouzane, France. (bertrand.chapron@ifremer.fr)

J. Johannessen, Nansen Environmental and Remote Sensing Center, Thormøhlensgate 47, N-5006 Bergen, Norway. (johnny.johannessen@nersc.no)